

MICROCOPY RESOLUTION TEST CHART  
NATIONAL BUREAU OF STANDARDS-1963-A

AD-A165 207



Report R85-956634-6

# VISCID/INVISCID INTERACTION ANALYSIS OF SUBSONIC TURBULENT TRAILING-EDGE FLOWS

by

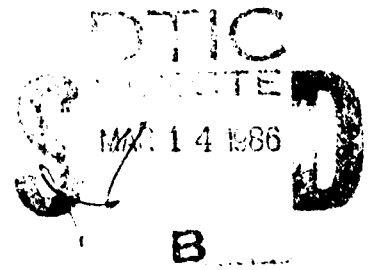
Mark Barnett and Joseph M. Verdon

Final Report

Prepared Under Contract N00014-83-C-0430

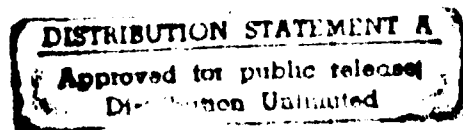
for the

Naval Air Systems Command  
Department of the Navy  
Washington, D.C. 20361



DTIC FILE COPY

December 1985



REPORT DOCUMENTATION PAGE

1a. REPORT SECURITY CLASSIFICATION <b>Unclassified</b>		1b. RESTRICTIVE MARKINGS	
2a. SECURITY CLASSIFICATION AUTHORITY		3. DISTRIBUTION / AVAILABILITY OF REPORT Approval for Public Release; distribution unlimited	
2b. DECLASSIFICATION / DOWNGRADING SCHEDULE			
4. PERFORMING ORGANIZATION REPORT NUMBER(S) UTRC Report R85-956634-6		5. MONITORING ORGANIZATION REPORT NUMBER(S)	
6a. NAME OF PERFORMING ORGANIZATION United Technologies Research Center	6b. OFFICE SYMBOL (if applicable)	7a. NAME OF MONITORING ORGANIZATION Turbopropulsion Laboratory, Code 67SF	
6c. ADDRESS (City, State, and ZIP Code) Silver Lane East Hartford, CT 06108		7b. ADDRESS (City, State, and ZIP Code) Naval Postgraduate School Monterey, CA 93940	
8a. NAME OF FUNDING / SPONSORING ORGANIZATION Naval Air Systems Command	8b. OFFICE SYMBOL (if applicable)	9. PROCUREMENT INSTRUMENT IDENTIFICATION NUMBER	
8c. ADDRESS (City, State, and ZIP Code) Department of the Navy Washington, D.C. 22202		10. SOURCE OF FUNDING NUMBERS	
		PROGRAM ELEMENT NO.	PROJECT NO.
		TASK NO.	WORK UNIT ACCESSION NO.
11. TITLE (Include Security Classification) Viscid/Inviscid Interaction Analysis of Subsonic Turbulent Trailing-Edge Flows			
12. PERSONAL AUTHOR(S) Mark Barnett and Joseph M. Verdon			
13a. TYPE OF REPORT Final Report	13b. TIME COVERED FROM 9/83 TO 7/85	14. DATE OF REPORT (Year, Month, Day) December 1985	15. PAGE COUNT 60
16. SUPPLEMENTARY NOTATION Final Report. Project Manager: R. P. Shreeve, Turbopropulsion Laboratory, Code 67SF, Naval Postgraduate School, Monterey, CA 93940			
17. COSATI CODES		18. SUBJECT TERMS (Continue on reverse if necessary and identify by block number)	
FIELD	GROUP	SUB-GROUP	
		Subsonic Turbulent Mean Flow; Viscid/Inviscid Interaction; Trailing-Edge/Near-Wake Region; Quasi-Simultaneous Viscid/Inviscid Coupling Procedure.	
19. ABSTRACT (Continue on reverse if necessary and identify by block number) Subsonic turbulent flow past thin-airfoil trailing edges is studied using a finite Reynolds number viscid/inviscid interaction model. Here, the flow in the outer or inviscid region is governed by the equations of linearized potential flow theory, while that in the inner or viscous region is governed by Prandtl's boundary-layer equations cast in terms of Levy-Lees variables. The effects of turbulence are represented using an algebraic turbulence model based on the eddy viscosity concept. The flow in the vicinity of the local strong interaction is determined by iteratively matching the solutions in the inviscid and viscous regions using a quasi-simultaneous coupling procedure. Turbulent mean-flow solutions have been obtained for a range of symmetric and asymmetric wedge-shaped trailing-edge geometries. Results illustrating the effects of airfoil thickness and loading on the detailed mean-flow behavior in the trailing-edge/near-wake region are presented.			
20. DISTRIBUTION / AVAILABILITY OF ABSTRACT <input checked="" type="checkbox"/> UNCLASSIFIED/UNLIMITED <input type="checkbox"/> SAME AS RPT <input type="checkbox"/> DTIC USERS		21. ABSTRACT SECURITY CLASSIFICATION	
22a. NAME OF RESPONSIBLE INDIVIDUAL		22b. TELEPHONE (Include Area Code)	22c. OFFICE SYMBOL

Viscid/Inviscid Interaction Analysis of  
Subsonic Turbulent Trailing-Edge Flows

TABLE OF CONTENTS

	<u>Page</u>
SUMMARY . . . . .	1
INTRODUCTION . . . . .	3
PROBLEM DESCRIPTION AND FORMULATION . . . . .	5
THE INVISCID REGION . . . . .	7
THE VISCOUS LAYER . . . . .	9
Turbulence Model . . . . .	11
NUMERICAL SOLUTION PROCEDURES . . . . .	15
Inviscid Surface Pressure . . . . .	16
Viscous Layer . . . . .	18
Quasi-Simultaneous Coupling Procedure . . . . .	20
NUMERICAL RESULTS . . . . .	23
Symmetric Trailing-Edge Flows . . . . .	25
Asymmetric Trailing-Edge Flows . . . . .	26
Streamlines for Laminar and Turbulent Mean Flows . . . . .	29
CONCLUDING REMARKS . . . . .	31
REFERENCES . . . . .	33
LIST OF FIGURES . . . . .	36
FIGURES	







## INTRODUCTION

For flows of practical interest in either external or internal aerodynamics the Reynolds number is usually sufficiently high so that the flow over an airfoil or blade can be divided into two regions: an "inner" dissipative region consisting of the boundary layer and wake, and an "outer" inviscid region. The principle interaction between the viscous and inviscid regions arises from the displacement thickness effect which leads to a thickened semi-infinite equivalent body with corresponding changes in surface pressure. If the interaction is "weak", i.e., the viscous effect on the pressure is small, the complete flow problem can be solved sequentially. This traditional approach for calculating the interaction between the viscous and inviscid parts of the flow is based on a direct hierarchy between the two regions, which is applicable as long as the disturbances to the inviscid flow due to the displacement effect are small.

In reality, the flow over an airfoil involves both a weak overall interaction arising from standard displacement effects, and also from wake curvature effects, and local strong viscous/inviscid interactions which arise due to rapid changes in geometry or boundary conditions. In particular, at an airfoil trailing edge a strong interaction arises from the abrupt change from the no-slip boundary condition on the airfoil surface to a streamline tangency (slip) boundary condition in the wake. Such features lead to singularities in a classical boundary-layer solution and a subsequent breakdown of a weak-interaction solution procedure. In addition, rapid changes in the displacement thickness in the strong-interaction region cause substantial changes in the local inviscid pressure field. The concept of an inner viscous region and an outer inviscid region still holds, but the classical hierarchical structure of the flow no longer applies. Thus in a local strong-interaction region the hierarchy changes from direct (i.e., pressure determined by the inviscid flow) to interactive (i.e., pressure determined by a mutual interaction between the inviscid flow and the viscous layer) and this change must be accommodated in the development of a local solution procedure.

In this report an analytical procedure based on finite Reynolds number viscous/inviscid interaction theory is presented for predicting subsonic turbulent flow past an airfoil trailing edge. The present effort is a continuation of the work reported in Refs. 1 and 2, where subsonic laminar flows past thin airfoil trailing edges are considered. The approach taken employs an interacting boundary-layer model. In this model the flow in the outer inviscid region is assumed to be potential and that in the inner region is assumed to be governed by Prandtl's boundary-layer equations, which are written in similarity-type variables. Inverse solutions to the finite-difference viscous-layer equations are determined by a superposition procedure, which is a particularly convenient technique for solving for the flow in an asymmetric wake. The solutions in the inviscid and viscous regions are matched through a quasi-simultaneous coupling

procedure using global iteration to obtain a converged result for the complete flow field. Our intention is to provide an accurate and dependable numerical scheme for predicting strong trailing-edge interactions and to elucidate turbulent flow behavior in airfoil trailing-edge/near-wake regions. Therefore we have attempted to obtain viscid/inviscid solutions on highly refined numerical grids and by using a rather stringent convergence criterion for the global viscid/inviscid iteration procedure.

In Refs. 1 and 2 solutions are presented for subsonic laminar attached and separated trailing-edge flows. In particular, separated laminar-flow solutions are presented in which local symmetric reverse-flow regions extend over twenty percent of airfoil chord and one-sided reverse-flow regions (adjacent to the airfoil suction surface) extend over ten percent of airfoil chord. We mention also the related studies, based on the asymptotic triple-deck ( $Re \rightarrow \infty$ ) model, by Smith (Refs. 3 and 4), who determined numerical solutions for separated flow past symmetric and asymmetric airfoil configurations, and was the first to demonstrate that one-sided closed laminar separation bubbles at a loaded subsonic trailing edge could be predicted using viscid/inviscid interaction theory. Later Elliott and Smith (Ref. 5) determined similar solutions for supersonic trailing edges. In addition, Veldman (Ref. 6) and Veldman and Lindhout (Ref. 7) have obtained results for laminar and turbulent trailing-edge separations using a finite-Re interacting boundary-layer model.

The numerical results obtained herein for turbulent flow demonstrate the behavior of the flow in the trailing-edge/near-wake region for thin loaded and unloaded airfoils. As would be expected, the turbulence strongly influences the behavior of the mean flow, particularly with regard to the separation of the viscous layer. This is demonstrated rather dramatically by the laminar and turbulent results obtained for the same symmetric and asymmetric trailing-edge configurations. The turbulent flow results indicate that such flows remain attached to the airfoil surface over a much wider range of airfoil geometries than those determined in Refs. 1 and 2 for high Reynolds number laminar flows.

## PROBLEM DESCRIPTION AND FORMULATION

In the following discussion the flow variables and spatial coordinates are dimensionless. Lengths have been scaled with respect to the length of the airfoil  $L^*$ , density, velocity and viscosity with respect to their free-stream values,  $\rho_\infty^*$ ,  $U_\infty^*$  and  $\mu_\infty^*$ , respectively, pressure with respect to twice the free-stream dynamic pressure,  $\rho_\infty^* U_\infty^{*2}$ , and temperature with respect to the square of the free-stream speed divided by the specific heat at constant pressure,  $U_\infty^{*2}/C_p^*$ . Here the superscript \* denotes a dimensional quantity and the subscript  $\infty$  refers to the free-stream conditions at infinity.

We consider high Reynolds number ( $Re = \rho_\infty^* U_\infty^* L^* / \mu_\infty^*$ ) adiabatic turbulent flow, with negligible body forces, of a perfect gas with constant specific heats, linear viscosity law and unit molecular and turbulent Prandtl numbers, past the trailing edge of an airfoil (Fig. 1). The flow is two-dimensional (in the  $x, y$ -plane) and subsonic with free-stream velocity,  $U_\infty^*$ , in the positive  $x$ -direction. The airfoil is thin and slightly cambered and it is located mainly along the interval  $[0,1]$  of the  $x$ -axis. Viscous effects are concentrated in relatively thin layers adjacent to the airfoil surfaces which merge into a thin wake behind the airfoil. The position of the upper and lower surfaces of the airfoil and wake displacement body are defined by

$$\begin{aligned} y_{\pm}(x) &= h_{\pm}(x) \pm \delta_{\pm}(x), & x \in [0,1] \\ &= h_W(x) \pm \delta_{\pm}(x), & x > 1 \end{aligned} \quad (1)$$

where  $h_+$  and  $h_-$  define the locations of the upper and lower surfaces of the airfoil,  $h_W$  defines the location of the reference wake streamline, and  $\delta_+$  and  $\delta_-$  are the upper- and lower-surface viscous displacement thicknesses (Fig. 1), respectively. Note that in Fig. 1 the symbols  $\mathcal{S}$ ,  $\mathcal{D}$  and  $\mathcal{W}$  refer to the airfoil surface, the displacement surface and the reference wake streamline, respectively. The latter is an arbitrary curve which emanates from the trailing edge of the airfoil and lies within the actual viscous wake. Under the stated assumptions concerning airfoil shape and flow Reynolds number, the projection of the airfoil and wake displacement body on the  $y$ -axis will be small (i.e., of  $O(\epsilon) \ll 1$ ).

Solutions will be determined for the flow in the trailing-edge region of the airfoil using finite  $Re$ , viscid/inviscid interaction concepts. If the outer inviscid flow is assumed to be isentropic and irrotational, then a velocity potential  $\phi = U_\infty x + \phi$  exists where the first-order (in  $\epsilon$ ) or disturbance potential can be determined by the methods of linearized potential flow theory. The flow in the inner or viscous region is assumed to be governed by Prandtl's boundary-layer equations which, to within the order of approximation considered here, can be solved in terms of coordinates parallel and normal to the free-stream direction. The effects of turbulence are incorporated by using the algebraic eddy-viscosity model due to Cebeci and Smith (Ref. 8) for surface boundary layers and the near-wake turbulence model of Cebeci, et al. (Ref. 9) which has been modified in the present study to permit the calculation of asymmetric wakes.

In the present analysis viscous displacement effects at the trailing edge are regarded as "strong", while wake curvature effects are regarded as "weak". This treatment is in accordance with the triple-deck scaling requirements for laminar flow at asymptotically large Reynolds number (Ref. 10). It is assumed, for lack of a correspondingly well-developed theory for turbulent flow, that this treatment can be extended to the turbulent problem. Thus, iterative solutions of the coupled inviscid and viscous equations will be repeatedly determined to obtain a converged solution which accounts for strong-displacement interactions, and the solution resulting from this procedure will then be corrected to account for wake curvature interactions. In the quasi-simultaneous procedure used in solving the strong-interaction problem, the viscid and inviscid solutions are coupled at each streamwise station on the airfoil and in the wake. This leads to a relatively fast convergence of the global iteration procedure as compared to the convergence achieved using the so-called semi-inverse procedure, which is frequently employed for viscid/inviscid interaction problems.

## THE INVISCID REGION

The disturbance potential is governed by the linear equation

$$(1-M_\infty^2) \phi_{xx} + \phi_{yy} = 0, \quad (2)$$

where  $M$  is the Mach number. In addition, the pressure  $P$  is related to the potential using Bernoulli's equation, i.e.,

$$P = P_\infty + p = (\gamma M_\infty^2)^{-1} - \phi_x. \quad (3)$$

Here  $P_\infty = (\gamma M_\infty^2)^{-1}$  is the free-stream pressure,  $p$  is the first-order or disturbance pressure, and  $\gamma$  is the specific heat ratio of the fluid.

The inviscid flow is determined as a solution of Eq. (2) which is subject to a flow tangency condition at the airfoil displacement surface, jump conditions on normal velocity and pressure across the wake, and the condition of uniform flow in the far field. Since first-order airfoil-surface and wake boundary conditions can be referred to the  $x$ -axis, it follows that

$$\phi_y|_{y=0^\pm} = [h_\pm(x) \pm \delta_\pm(x)]' \quad \text{for } x \in [0,1], \quad (4)$$

$$[\phi_y] = \delta_W'(x) \quad \text{and} \quad [p] = \kappa(x)[\delta_W(x) + \theta_W(x)] \quad \text{for } x > 1, y=0, \quad (5)$$

and

$$\nabla\phi \rightarrow 0 \quad \text{as } |x| \rightarrow \infty. \quad (6)$$

Here the prime denotes differentiation,  $[ ]$  denotes the difference (upper minus lower) in a quantity across the wake,  $\delta_W$  and  $\theta_W$  are the displacement and momentum thicknesses, respectively, of the complete wake, and  $\kappa$  is the curvature (positive - concave upwards) of the reference wake streamline. A complication arises in that the location, and hence the curvature, of the reference wake streamline is not known a priori; however, to within lowest order in  $\epsilon$  the wake can be represented by an arbitrary curve which emanates from the trailing edge of the airfoil and lies within the actual viscous wake.

The solution,  $\phi(x,y)$ , to the foregoing boundary-value problem can be determined conveniently using complex variable theory and, in particular, Cauchy's integral formula. We refer the reader to Ref. 11 and Refs. 1 and 2 for more complete details, and list here only those results pertaining to the first-order pressure acting on the airfoil surface. This pressure can be expressed in the form

$$\begin{aligned} p(x,0^\pm) &= p_D(x,0^\pm) \pm \left[ p_{WC}^A(x) \right] / 2 \\ &= p^S(x,0) \pm \left[ p_D^A(x) \right] / 2 \pm \left[ p_{WC}^A(x) \right] / 2, \quad x \in [0,1], \end{aligned} \quad (7)$$

where the superscripts + and - refer to the upper and lower surfaces, respectively, of the airfoil displacement body;  $p_D(x,0^\pm)$  is the first-order surface pressure due to displacement (airfoil + viscous) effects,  $p^S(x,0)$  is the symmetric component of this pressure due to the displacement-body thickness;  $\left[ p_D^A \right]$  is the jump in pressure across the airfoil due to displacement-body camber; and  $\left[ p_{WC}^A \right]$  is the jump in pressure across the airfoil due to wake curvature. The terms on the right-hand-side of Eq. (7) can be evaluated from the following expressions:

$$p^S(x,0) = - \frac{1}{\pi(1-M_\infty^2)^{1/2}} \oint_0^\infty \frac{D_T'(\zeta)}{x-\zeta} d\zeta; \quad (8)$$

$$\left[ p_D^A \right] = \frac{-2}{\pi(1-M_\infty^2)^{1/2}} \left( \frac{1-x}{x} \right)^{1/2} \oint_0^1 \frac{D_C'(\zeta)}{x-\zeta} \left( \frac{\zeta}{1-\zeta} \right)^{1/2} d\zeta; \quad (9)$$

and

$$\oint_0^1 \frac{\left[ p_{WC}^A(\zeta) \right]}{x-\zeta} d\zeta = - \int_1^\infty \frac{\kappa(\zeta) [\delta_W(\zeta) + \theta_W(\zeta)]}{x-\zeta} d\zeta. \quad (10)$$

Here the symbol  $\oint$  denotes a Cauchy principle-value integral,  $D_T = (y_+ - y_-)/2$  is one-half of the displacement-body thickness, and  $y = D_C = (y_+ + y_-)/2$  defines the location of the displacement-body camber line. In Eq. (10) the wake curvature  $\kappa$  is taken to be the curvature of the inviscid wake camber line as determined from the strong-displacement interaction inviscid solution; i.e.,

$$\kappa(x) = D_C''(x) = \frac{(1-M_\infty^2)^{1/2}}{2\pi} \frac{d}{dx} \int_0^1 \frac{\left[ p_D^A(\zeta) \right]}{x-\zeta} d\zeta, \quad x > 1. \quad (11)$$

## THE VISCOUS LAYER

For thin airfoils operating at high Reynolds number the viscous-layer equations (i.e., Prandtl's boundary-layer equations) can be written in terms of coordinates parallel ( $x$ ) and normal ( $y$ ) to the free stream direction. First Prandtl's transformation; i.e.,

$$\tilde{y}_{\pm} = \pm \text{Re}^{1/2} (y - h_{\pm})$$

and

$$\tilde{v}_{\pm} = \pm \text{Re}^{1/2} (v - u h'_{\pm})$$

is introduced, where  $h_+ = h_- = h_w$  for  $x > 1$ ,  $u$  and  $v$  are the velocity components in the  $x$  and  $y$ -directions, and the scaled normal coordinate  $\tilde{y}$  and normal velocity component  $\tilde{v}$  are positive along the outward normal to the  $x$ -axis. To facilitate their numerical resolution, we recast the viscous equations in terms of Levy-Lees variables. Use of these variables leads to a reduction in numerical truncation error because streamwise gradients of the dependent flow variables are minimized, and also gives a better account of the growth of the viscous-layer allowing one to use a fixed number of grid points in the normal direction (see Davis and Werle, Ref. 12). In addition, the Levy-Lees variables admit convenient similarity solutions for an important class of laminar flows.

Thus with new independent ( $\xi$  and  $\eta$ ) and dependent ( $F$  and  $V$ ) variables defined by

$$\xi = \xi_I + \int_{x_I}^x \rho_e \mu_e u_e g dx, \quad \eta = \frac{u_e}{\sqrt{2\xi}} \int_0^{\tilde{y}} \rho d\tilde{y} \quad (13)$$

and

$$F = u/u_e, \quad V = 2\xi \left[ F \frac{\partial \eta}{\partial x} + \rho \tilde{v} \sqrt{\text{Re}} (2\xi)^{-1/2} \right] / \frac{d\xi}{dx}; \quad (14)$$

the viscous equations assume the form

$$2\xi \frac{\partial F}{\partial \xi} + \frac{\partial V}{\partial \eta} + F = 0 \quad (15)$$

and

$$2\xi F \frac{\partial F}{\partial \xi} + V \frac{\partial F}{\partial \eta} + \beta(F^2 - 1) - \frac{\partial}{\partial \eta} \left( \ell \frac{\partial F}{\partial \eta} \right) = 0, \quad (16)$$

where

$$\beta = \frac{2\xi}{u_e} \frac{du_e}{d\xi} \left( 1 + \frac{u_e^2}{2T_e} \right) = \frac{2\xi}{M_e} \frac{dM_e}{d\xi} \quad (17)$$

and

$$\ell = \rho\mu (1 + \gamma_{Te}) / (\rho_e \mu_e g). \quad (18)$$

In Eqs. (13) through (18) the subscript e refers to the edge of the viscous layer,  $\rho$  and  $\mu$  are the fluid density and viscosity respectively,  $\gamma_T$  is a streamwise intermittency factor which will be assumed simply to be unity, and  $e$  is the turbulent eddy viscosity, which will be discussed in detail below. The quantity  $g(x)$  appearing in Eqs. (13) and (18) was employed in Ref. 13. It is specified so that the coefficient  $\ell$ , defined in Eq. (18), is approximately equal to one over most of the viscous layer; it appears in the definition of  $\xi$  in order to maintain a nearly constant  $\eta$  value for the edge of the boundary layer in turbulent flow. Fluid properties at the edge of the viscous layer (i.e., inviscid properties at the displacement surface,  $\eta$ ) are determined from Bernoulli's equation and the isentropic relations for a perfect gas. Note that as a consequence of our original assumptions, the total enthalpy is constant throughout the field and therefore only the continuity and momentum equations, Eqs. (15) and (16), must be solved to determine the flow in the viscous layer.

The boundary conditions on  $F$  and  $V$  are as follows:

$$F \rightarrow 1 \quad \text{for } \eta \rightarrow \infty, \quad (19)$$

$$F = V = 0 \quad \text{for } \xi \leq \xi_{TE}, \quad \eta = 0, \quad (20)$$

and

$$v = 0 \quad \text{for} \quad \xi > \xi_{TE}, \quad \eta = 0. \quad (21)$$

Condition (21) follows from the requirement that the velocity component normal to the reference wake streamline must be zero. For convenience, the subscripts + and - have been omitted from Eqs. (13) through (21).

To determine the effect of the viscous layer on the outer flow, the displacement and momentum thicknesses must be evaluated from the upper- and lower-surface viscous solutions. It follows from the standard definitions of the displacement thickness,  $\delta$ , and the momentum thickness,  $\theta$ , that

$$\rho_e u_e \delta (Re/2\xi)^{1/2} = \int_0^{\infty} \left[ 1 - F + \frac{(\gamma-1)}{2} M_e^2 (1-F^2) \right] d\eta \quad (22)$$

and

$$\rho_e u_e \theta (Re/2\xi)^{1/2} = \int_0^{\infty} (1-F) F d\eta. \quad (23)$$

The displacement and momentum thicknesses of the complete wake are then given by

$$\delta_W = \delta_+ + \delta_- \quad \text{and} \quad \theta_W = \theta_+ + \theta_- . \quad (24)$$

#### Turbulence Model

At high Reynolds number the flow in the the viscous-layer is mostly turbulent. In particular, the flow usually undergoes a transition from laminar to turbulent near the leading edge of the airfoil. Thus, in order to simulate real flows, a turbulence model is generally required. In the present study we employ the eddy-viscosity model developed by Cebeci and Smith (Ref. 8) for airfoil boundary layers and subsequently modified by Cebeci, et al. (Ref. 9) for near-wake flows.

In this model the turbulent boundary layer is viewed as consisting of two distinct regions, an inner one and an outer one. The eddy viscosity in the inner and outer regions is given (in terms of Levy-Lees variables) by

$$e = \begin{cases} e_i = 0.16 D^2 (2\xi Re)^{1/2} \rho^2 \theta^2 \mu^{-1} |\partial F / \partial \eta| & \text{for } \eta < \eta_1 \\ e_o = 0.0168 \rho \mu^{-1} (2\xi Re)^{1/2} \left| \int_0^\infty \frac{1-F}{\rho} d\eta \right| & \text{for } \eta \geq \eta_1 \end{cases} \quad (25)$$

respectively, where  $\eta_1$  is defined as the smallest value of  $\eta$  for which  $e_o = e_i$ . Here

$$D = 1 - \exp\left(\frac{-\sqrt{2\xi}}{a u_e} \int_0^\eta \frac{d\eta}{\rho}\right) \quad (26a)$$

where the length scale,  $a$ , is given by

$$a = 26\mu / [\rho Re^{1/2} (1 - 11.8 p^+)^{1/2} u_\tau] \quad (26b)$$

and the pressure gradient  $p^+$  and shear velocity  $u_\tau$  are defined by

$$p^+ = (\mu_e u_e)^2 g \frac{du_e}{d\xi} / (Re u_\tau^3) \quad (26c)$$

and

$$u_\tau = u_e (2\xi Re)^{-1/4} \left[ \mu \frac{\partial F}{\partial \eta} \right]_{\eta=\eta_m}^{1/2} = (C_f / \rho_w)^{1/2} \quad (26d)$$

respectively. In Eq. (26d)  $\eta_m$  is taken to be the value of  $\eta$  at which  $\mu \partial F / \partial \eta$  reaches a maximum value. This modification to the usual definition of  $u_\tau$ , in which  $\eta_m$  is set to zero, was introduced in Ref. 14, and is applied here to avoid spurious skin-friction predictions in the vicinity of boundary layer separation and re-attachment points.

In the turbulent wake the inner region is further subdivided into two parts.

Thus

$$e = \begin{cases} e_w = 0.4 \frac{\rho}{\rho(\eta_c)} \frac{\mu(\eta_c)}{\mu} \exp\left[\frac{u_e F(\eta_c)}{2.75 u_{\tau E}} - 2.08\right] & \text{for } 0 < \eta < \eta_2 \\ e_i & \text{for } \eta_2 \leq \eta < \eta_1 \end{cases} \quad (27)$$

where  $\eta_c$  is the value of  $\eta$  such that

$$\int_0^{\eta} \frac{d\eta}{\rho} = \frac{u_e \mu(\eta)}{\sqrt{2\xi Re} u_{\tau E} \rho(\eta)} \exp\left[\frac{u_e F(\eta)}{2.75 u_{\tau E}} - 2.08\right]. \quad (28)$$

In Eq. (28)  $F(\eta)$  is the computed velocity profile in the wake and  $u_{\tau E}$  is the shear velocity at a cusped trailing edge or at a specified location upstream of the trailing edge for a wedge-shaped trailing edge, or, if the flow separates, at a point upstream of the separation point. The value of  $\eta_2$  is determined from the condition that  $e_w = e_i$  at  $\eta_2$ . For  $\eta_2 < \eta < \eta_1$ , the first of Eqs. (25) is applied with  $D = 1$ . To prevent  $e_w$  from exceeding  $e_o$  at large distances downstream of the trailing edge, once  $e_o = e_w$  the eddy viscosity for larger values of  $\xi$  is assumed to be the local value of  $e_o$  across the boundary layer.

The foregoing model was developed for symmetric wakes. To compute asymmetric wakes a modified version was applied. In this version the value of  $e_w$  was calculated by referring all quantities previously referenced to the wake centerline (reference wake streamline for symmetric flows) to the locus of the minimum streamwise velocities. In general, this procedure leads to a discontinuity in  $e_w$  across this locus, since  $e_w$  will be different on the two sides of the wake. However, for the cases calculated here, the discontinuity was found to be quite small. Similarly, the inner eddy viscosity,  $e_i$ , in the wake is computed using quantities referenced to the minimum velocity locus. The incompressible displacement thickness appearing in the expression for the outer eddy viscosity has been calculated relative to the reference wake streamline ( $\eta = 0$ ). Although this quantity could also have been determined relative to the minimum velocity locus, since the distance between the wake streamline and the locus of the minimum streamwise velocities is small, this would make little difference in the final result. As the flow proceeds downstream it returns to a symmetric state. Therefore, although there might be a small discontinuity in  $e_o$  across the locus of minimum velocity, it will disappear with increasing distance downstream from the airfoil.

The foregoing modifications to the wake turbulence model of Ref. 9 were considered adequate for the present asymmetric flow calculations. However, these changes should only be viewed as provisional, until a more rational near-wake turbulence model becomes available. One possible alternative to the turbulence model used here for asymmetric flows is discussed in Ref. 15.

## NUMERICAL SOLUTION PROCEDURES

A solution for the complete flow field is determined by matching the solutions to the inviscid and viscous equations. In the present analysis iterative solutions of the inviscid and viscous equations are determined to account for strong-displacement interactions and the resulting inviscid solution is then corrected to account for wake curvature interactions. Strong-interaction effects are determined using a global iteration procedure. Here the displacement thickness distribution,  $\delta^n(x)$ , for the  $(n+1)$ th iteration level is prescribed, and the inviscid and viscous equations are solved to determine an intermediate displacement thickness distribution,  $\delta^{n+1/2}(x)$ . The  $(n+1)$ th distribution,  $\delta^{n+1}(x)$ , is estimated according to the relation

$$\delta^{n+1} = \omega \delta^{n+1/2} + (1-\omega)\delta^n \quad (29)$$

where  $\omega$  is a relaxation parameter. This process is repeated until the maximum difference between  $\delta^{n+1}(x)$  and  $\delta^n(x)$  over all streamwise mesh stations satisfies a specified convergence criterion.

In Refs. 1 and 2 a semi-inverse global iteration procedure was used to determine the flow in strong viscous/inviscid interaction regions. In this approach the inviscid and viscous equations are solved independently at each level of the iteration procedure to determine an inviscid pressure distribution,  $p_{inv}(x)$ , at the displacement surface, and a viscous pressure distribution,  $p_{visc}(x)$ , in the viscous-layer. The  $(n+1/2)$  estimate for the displacement thickness is then obtained using the global iteration formula developed by Carter Ref. 16; i.e.,

$$\delta^{n+1/2}(x) = \delta^n(x) \left[ 1 + \left[ \frac{p_{inv}^{n+1}(x) - p_{visc}^{n+1}(x)}{p_{inv}^{n+1}(x)} \right] \right]. \quad (30)$$

Equations (30) and (29) are applied to update the displacement thickness distributions for the boundary layers on the upper and lower surfaces of the airfoil and for the complete wake.

The semi-inverse procedure is generally satisfactory, giving reasonable convergence rates for attached flows, but it requires a prohibitive number of iterations using substantial underrelaxation ( $\omega < 1$ ) to achieve converged solutions for separated flows. The stability analysis of Wigton and Holt, Ref. 17, indicates that the semi-inverse procedure will encounter stability problems for large

displacement thickness gradients and/or for small streamwise mesh spacings, such as those required to resolve the flow at the trailing edge of an airfoil or in a local reverse-flow region. A numerical demonstration of this stability problem is given by Edwards and Carter Ref. 18.

An attractive alternative to the semi-inverse procedure is the so-called quasi-simultaneous coupling procedure of the type introduced by Veldman Ref. 19. Several methods for implementing the quasi-simultaneous procedure have been developed and applied to the calculation of strong-interaction flow fields (e.g., see Veldman Refs. 6, 7, Edwards and Carter Ref. 18, Davis Ref. 20, Le Balleur and Girodroux-Lavigne Ref. 21). Here, at each level of the global iteration, the viscous and inviscid solutions are coupled locally at each streamwise station in the strong-interaction region. Thus, instead of solving the viscous and inviscid flows separately for a prescribed displacement thickness distribution and then using a relaxation formula like Eq. (30) to update the displacement thickness, the viscous and inviscid equations are solved simultaneously. Global iterations on the displacement thickness distribution are still required, but the convergence rate of the iteration procedure is considerably enhanced over that achieved with a semi-inverse calculation. This is demonstrated in the results presented in Ref. 18 where the convergence rates of the semi-inverse and quasi-simultaneous methods are compared.

The semi-inverse global iteration procedure was employed in Refs. 1 and 2 to predict laminar attached and separated trailing-edge flows. Consistent with the observations reported in Ref. 18, and the stability analysis of Ref. 17, the convergence rate was found to decrease as the displacement thickness increased, and severe underrelaxation was necessary to predict flows with large separated regions. Based upon these observations, and the demonstrated improvement in convergence rates possible with the quasi-simultaneous solution procedure, the latter has been adopted for the present investigation of turbulent trailing-edge flows. The details of the present implementation of the quasi-simultaneous procedure will be given below, but first we outline the numerical methods used to solve the equations governing the flow in the inviscid region and in the viscous layer.

#### Inviscid Surface Pressure

We require numerical solutions for the first-order inviscid surface pressure and the viscous displacement thickness over a strong-interaction solution interval extending from  $x = x_I$  to  $x = x_F$ . First, we consider the inviscid solution. The integral appearing in Eq. (8) for the symmetric component of the pressure is here approximated over the strong-interaction solution domain by a trapezoidal-rule quadrature, i.e.,

$$\int_{x_{IB}}^{x_{IE}} \frac{D_T'(\zeta)}{x_i - \zeta} d\zeta \approx \sum_{j=IB}^{IE-1} D_T'(\bar{x}_j) \frac{x_{j+1} - x_j}{x_i - \frac{1}{2} \bar{x}_j} \quad (31)$$

where  $i$  and  $j$  are streamwise mesh point indices,  $IB$  and  $IE$  refer to the mesh stations at the beginning and end of the strong-interaction solution domain respectively (i.e., at  $x_I$  and  $x_F$ ), and  $\bar{x}_j = (x_{j+1} + x_j)/2$ . This representation for the symmetric integral corresponds to the discretization used by Veldman, Ref. 19, and is accurate to first-order in  $\Delta x$ , as opposed to the second-order accurate representation used in Ref. 2. The reason for choosing this particular discretization for the symmetric integral will be discussed below. Although neglected here, contributions to the local (at  $x = x_i$ ) pressure due to thickness effects from upstream ( $0 < \zeta < x_I$ ) and downstream (at  $\zeta > x_F$ ) of the strong-interaction region can be determined by analytical or numerical integration (using trapezoidal-rule quadrature) depending upon the assumed functional form of the thickness distribution,  $D_T(x)$ .

It is somewhat more difficult to determine the pressure difference component,  $[p_D^A]$ , because of the singular term  $[\zeta/(1-\zeta)]^{1/2}$  which appears inside the integral on the right-hand-side of Eq. (9). However, a first-order accurate approximation to this integral has been determined in Refs. 1 and 2 and is given by

$$\int_0^1 \frac{D_c'(\zeta)}{x_i - \zeta} \left(\frac{\zeta}{1-\zeta}\right)^{1/2} d\zeta \approx \sum_{j=IB}^{IT-2} D_c'(x_{j+1}) I(x_i, \bar{x}_j, \bar{x}_{j+1}) + D_c'(1) I(x_i, x_{IT-1}, 1) \quad (32)$$

where the subscript  $IT$  refers to the trailing-edge mesh line. The integral term  $I$  appearing in Eq. (32) is given by

$$I(x_i, \bar{x}_j, \bar{x}_{j+1}) = \int_{\bar{x}_j}^{\bar{x}_{j+1}} \frac{f(\zeta)}{x_i - \zeta} d\zeta \quad (33)$$

where  $f(\zeta) = [\zeta/(1-\zeta)]^{1/2}$ , and it can be evaluated in closed form.

Once a converged solution to the strong-displacement interaction problem is achieved, the pressure distribution must be corrected to account for wake curvature effects. The curvature of the reference wake streamline is determined by a

numerical approximation to Eq. (11). Since  $\kappa(x)$  must only be determined for  $x > 1$ , the integral on the right-hand-side of Eq. (11) can be evaluated by a simple trapezoidal-rule quadrature. The pressure difference across the airfoil due to wake curvature effects,  $[P_{WC}^A]$ , is then determined by a numerical solution of the integral equation (10). This Fredholm integral equation of the first kind can be conveniently solved by first transforming the interval  $[0,1]$  on the  $x$ -axis to the interval  $[0,\pi]$  in the unit circle and invoking certain properties of Chebyshev polynomials. We refer the reader to Ref. 1 for further details.

### Viscous Layer

The viscous-layer equations are solved in an inverse fashion (thus avoiding the separation singularity), since the pressure is not prescribed but must be determined in terms of an unknown displacement thickness distribution. Solutions for the boundary layers on the upper and lower surfaces of the airfoil and for the complete wake are determined by marching in the  $x$ - (or  $\xi$ ) direction. In each case the continuity and momentum equations are replaced by a set of linear algebraic equations using a finite difference approximation in which the nonlinear terms in the momentum equation for the  $(n+1)$ th iteration are linearized about the solution at the previous,  $(n)$ th, iteration and the  $\xi$ - and  $\eta$ -derivatives are replaced by one-sided and central difference expressions, respectively. An up-wind differencing scheme is used for the  $\xi$ -derivatives; i.e., backward differencing is used if  $F > 0$  and forward differencing is used if  $F < 0$ . This approach results in a stable numerical algorithm in the presence of reverse flow and should be more accurate than the commonly used FLARE approximation (Ref. 22) in which the streamwise convection terms are set to zero in reverse-flow regions.

The resulting set of linear difference equations is solved using a superposition technique. Essentially, the dependent variables,  $F$  and  $V$ , are decomposed into two components (e.g.,  $F = \beta F_I + F_{II}$ ) such that two sets of linear algebraic equations are obtained. The components of  $F$  and  $V$  are related through a viscous constraint relation, i.e.,

$$\beta = (I_b/2I_a) \left\{ \left[ 1 + 4I_a \left( I_c - \frac{\rho_e u_e \delta}{\sqrt{2\xi/Re}} \right) / I_b^2 \right]^{1/2} - 1 \right\} \quad (34)$$

which is obtained from the definition of the displacement thickness, Eq. (22), and after solving the resulting quadratic equation for  $\beta$  and eliminating the extraneous solution. The quantities  $I_a$ ,  $I_b$  and  $I_c$  in Eq. (34) are defined by

$$I_a = \frac{\gamma-1}{2} (M_e)^2 \int_0^{\infty} F_I^2 d\eta \quad (35a)$$

$$I_b = \int_0^{\infty} [1 + (\gamma-1)(M_e)^2 F_{II}] F_I d\eta \quad (35b)$$

and

$$I_c = \int_0^{\infty} [1 - F_{II} + \frac{\gamma-1}{2} (M_e)^2 (1 - F_{II}^2)] d\eta . \quad (35c)$$

The solution for an asymmetric viscous wake is obtained by treating the upper and lower sides of the wake simultaneously. A boundary condition is imposed on  $F$  at each edge (c.f. Eq. (19)), and a condition is imposed on  $V$  at the reference streamline (c.f. Eq. (21)). At the trailing edge of an asymmetric airfoil the upper- and lower-surface values of  $\xi$  and  $\eta$  differ from each other. For the wake calculation, one set of independent variables,  $\xi$  and  $\eta$ , is used. Therefore, to continue the boundary-layer solutions into the wake, the trailing-edge velocity profile on the lower surface of the airfoil is expressed in terms of upper-surface variables ( $\xi_+$ ,  $\eta_+$ ), so that a single set of independent variables can be employed for the wake calculation.

The definition for  $\xi$ , Eq. (13), contains the function  $g(\xi)$ , and, since  $g$  is generally on the order of 10 or more in turbulent flow, the upper- and lower-surface values of  $\xi$  at the trailing edge can differ significantly, as noted above. This difference can introduce inaccuracies into the numerical solution of a strongly asymmetric turbulent flow. In particular, if the discrepancy between the upper- and lower-surface values of  $\xi$  is large, the resolution accuracy for the near-wake shear layer coming off the pressure surface of the airfoil will be reduced by the redefinition of the lower-surface normal grid. To minimize this effect, the same value of  $g(\xi)$ ; i.e.,  $g(\xi) = (e_{o,+} + e_{o,-})/2$ , has been used for both the suction- and pressure-surface boundary-layer calculations, as well as in the wake. As a result of this procedure  $\xi_- = \xi_+ + O(\epsilon)$  at the trailing edge. Since the function  $g$  is only a scaling parameter, the foregoing procedure will not affect the boundary-layer solutions provided that the initial  $\eta$ -distributions of grid points is chosen so that a sufficient resolution (in the normal direction) of the boundary layers along both airfoil surfaces and of the wake is maintained.

## Quasi-Simultaneous Coupling Procedure

The quasi-simultaneous coupling procedure requires a local coupling of the inviscid and viscid solutions to determine the intermediate displacement thickness distribution ( $\delta^{n+1/2}$ ) at each global iteration level. In the present application this coupling is achieved by working with the two relations, Eqs. (17) and (34) for the pressure gradient parameter,  $\beta$ . In Eq. (17)  $\beta$  is defined in terms of the inviscid properties at the edge of the viscous layer, while in Eq. (34) it depends also on the details of the flow within the viscous layer. For thin-airfoil flow fields it follows from Eq. (17) and the inviscid relations which hold at the edge of the viscous layer, that to within first-order in  $\epsilon$  the pressure gradient parameter is given by

$$\beta = -2\xi \left( 1 + \frac{(\gamma-1)M_\infty^2}{2} \right) \frac{dp_D}{d\xi} \quad (36)$$

Note that only the first-order pressure due to strong displacement-interaction effects has been included in the foregoing expression for  $\beta$ .

To assist in describing the local coupling procedure for asymmetric flow, we introduce the integer index,  $k$ . For streamwise mesh stations ( $x$  (or  $\xi$ ) = constant) along the upper and lower surfaces of the airfoil, we set

$$k = 2(i-IB) + 1, \quad i = IB, IB+1, \dots, IT \quad (37a)$$

and

$$k = 2(i-IB) + 2, \quad i = IB, IB+1, \dots, IT, \quad (37b)$$

respectively; and for mesh stations along the wake, we set

$$k = i - IT + 2(IT-IB) + 2, \quad i = IT+1, IT+2, \dots, IE. \quad (37c)$$

Here  $IB$  and  $IE$  are the  $i$  indices corresponding to the stations at the beginning and end, respectively, of the strong-interaction solution domain and  $IT$  corresponds to the station at the trailing-edge point of the airfoil. The viscid/inviscid interaction solution at the  $n$ th global iteration level is obtained by marching from  $k = 3$  to  $k = KE = IE - IT + 2(IT - IB) + 2$ . Thus for  $i \leq IT$  the

solution at  $\xi = \xi_i$  is first updated on the upper surface of the airfoil and then on the lower surface, while for  $i > IT$  the solution is updated for the complete wake. Conditions at the beginning of the strong-interaction solution domain (i.e., at  $k = 1, 2$ ) are fixed and are obtained as a direct solution of the turbulent boundary-layer equations for a prescribed inviscid pressure gradient.

Discrete approximations to Eqs. (36) and (34) can be written in the form

$$\beta_k = \sum_{j=1}^k \alpha_{kj} \delta_j^{n+1/2} + \sum_{j=k+1}^{KE} \alpha_{kj} \delta_j^n + Q_k, \quad k=3, \dots, KE \quad (38)$$

and

$$\beta_k = (I_b/2I_a) \left\{ \left[ 1 + 4I_a \left( I_c - \frac{\rho_e u_e \delta_k^{n+1/2}}{\sqrt{2\xi}/Re} \right) / I_b^2 \right]^{1/2} - 1 \right\}, \quad k=3, \dots, KE \quad (39)$$

where the coefficients  $\alpha_{k,j}$  and  $Q_k$  are known and depend on the difference approximations used in Eqs. (31) and (32) to evaluate  $p_D$  and in Eq. (36) to evaluate  $dp_D/d\xi$ . The  $\delta_j^n$  are prescribed at the beginning of the  $n$ th global iteration for all  $j$ , and the  $\delta_j^{n+1/2}$  for  $j < k$  are determined by the current ( $(n+1)$ th) marching solution. Thus Eqs. (38) and (39) provide two relations for determining the values of  $\beta_k$  and  $\delta_k^{n+1/2}$  at the  $k$ th station. In the semi-inverse procedure used in Refs. 1 and 2 the  $\delta_j^{n+1/2}$  in Eqs. (38) and (39) are replaced by  $\delta_j^n$ , resulting in two solutions ( $\beta_{k_{inv}}$  and  $\beta_{k_{visc}}$ ,  $k = 3, \dots, KE$ ) for the pressure gradient parameter at each step of the global iteration procedure. These are then used to determine the  $(n+1)$ th estimate for the displacement thickness distribution (c.f. Eq. (30)). The local coupling of the inviscid and viscous solutions implied by Eqs. (38) and (39) requires more computational effort per iteration level than a semi-inverse calculation but, if properly constructed, it leads to a significant reduction in the number of global iterations required to determine a converged strong-interaction solution.

Once updated values of  $\delta_k$  (i.e.,  $\delta_k^{n+1/2}$ ) are determined, corresponding values of the inviscid flow properties ( $p_D$ ,  $u_e$ , etc.) are determined in terms of the  $\delta_j^{n+1/2}$  at  $j = 1, \dots, k$ , and the  $\delta_j^n$  at  $j = k+1, \dots, KE$ , and the viscous-layer variables  $F$  and  $V$  at station  $k$  are determined in terms of  $\beta_k$ . With this information the marching solution can be continued downstream. For symmetric flows

the foregoing procedure is considerably simplified since solutions are only required on either the upper or lower half-planes.

As pointed out by Veldman (Ref. 6) and Davis (Ref. 20), the matrix of influence coefficients,  $\alpha_{k,j}$  in Eq. (38), must be diagonally dominant for a successful implementation of the quasi-simultaneous coupling procedure. To achieve this we have employed the same discretization as used by Veldman (Ref. 19) for the symmetric pressure integral in Eq. (31) rather than the discretization used in our earlier work (Refs. 1 and 2) which yields a non-diagonally dominant matrix of influence coefficients. In addition, the quantities  $D_T'$  and  $D_C'$  in Eqs. (31) and (32) and the pressure gradient  $dp_D/d\xi$  in Eq. (36) have been evaluated using first-order accurate backward difference approximations. Finally, in the latter approximation the inviscid pressure at station  $k$  is assumed to depend on  $\delta_j^{n+1/2}$  for  $j = 3, \dots, k$  and  $\delta_j^n$  for  $j = k+1, \dots, KE$  while the pressure at the upstream station  $k-m$ , where, for asymmetric flow,  $m = 2$  for stations on the airfoil and  $m = 1$  for wake stations, is evaluated in terms of  $\delta_j^{n+1/2}$  for  $j = 3, \dots, k-m$  and  $\delta_j^n$  for  $j = k-m+1, \dots, KE$ . The counter  $m$  is equal to one on both the airfoil and the wake for symmetric flow.

In Ref. 6 Veldman extended his method to asymmetric flows. He noted that the discretization which was applied to the asymmetric integral on the left-hand side of Eq. (32) is not diagonally dominant. However, he found that, provided the grid is not excessively fine at the trailing edge, the solution is still convergent. In the present study, where the discretization of the asymmetric integral is different than Veldman's, but also not diagonally dominant, similar behavior is observed. All of the solutions for asymmetric flows obtained in the present study converged with a relaxation factor, in Eq. (29), of one. However, the convergence rate slowed as the grid was refined in the vicinity of the trailing edge, which is consistent with Veldman's observations and the analysis of Wigton and Holt (Ref. 17).

In the present numerical implementation of the viscous/inviscid iteration scheme, the viscous-layer equations are solved, as noted above, using a superposition technique. It was found that this technique, in conjunction with the quasi-simultaneous coupling procedure, leads to a very convenient method of solution for asymmetric wakes. The reason for this is that wakes and surface boundary layers can be solved in an identical manner, except that different boundary conditions are applied at  $\eta = 0$ .

## NUMERICAL RESULTS

The procedures outlined above have been applied to predict high Reynolds number turbulent flow in the trailing-edge and near-wake region of a thin airfoil. The airfoil geometry considered here is the same as that considered by Veldman in Ref. 6 and in our earlier work (Refs. 1 and 2) on laminar trailing-edge flows. The symmetric part of the airfoil (i.e., the thickness distribution) is constructed from circular-arc trailing-edge sections which are smoothly joined to flat sections which extend to the leading edge. For the purpose of analyzing local strong-interaction effects at the trailing edge there is no need to prescribe closure at the leading edge of the airfoil. The antisymmetric part of the airfoil (i.e., the camber distribution) is determined from a prescribed pressure jump across the airfoil. This geometry insures that the oncoming boundary layers will remain attached until or shortly before the trailing edge. For laminar flow, separation is encountered for relatively small amounts of thickness and camber. It was anticipated that a separated turbulent mean flow would not occur unless the airfoil thickness and/or camber was significantly more severe than that at which laminar separation occurs. This expectation is confirmed by our numerical results, as will be shown below.

The airfoil surfaces are located at

$$y_{\pm}(x) = h_{\pm}(x) = \pm D_{T,A}(x) + D_{C,A}(x), \quad x \in [0,1] \quad (40)$$

where  $2D_{T,A}$  defines the airfoil thickness distribution and  $D_{C,A}$  defines the location of the airfoil camberline. Here  $D_{T,A}$  is given by

$$\begin{aligned} D_{T,A}(x) &= T/2 & , \quad 0 \leq x < x_c \\ &= T/2 - R + \sqrt{R^2 - (x-x_c)^2} & , \quad x_c \leq x \leq 1 \\ &= 0 & , \quad x > 1 \end{aligned} \quad (41)$$

where  $T$  is the maximum thickness of the airfoil,  $R$  is the radius of curvature of the circular-arc trailing-edge sections, i.e.,

$$R = \frac{(T/2)^2 + (1-x_c)^2}{T}, \quad (42)$$

and  $x_c$  is the point at which these circular-arc sections are joined to the flat sections of the airfoil. The inviscid pressure jump across the airfoil,  $[p_A^A(x)]$ , is assumed to be constant upstream of the point  $x = x_c$  and equal to that acting on a flat plate inclined at angle  $\alpha$  relative to the uniform stream for  $x \leq x_c \leq 1$ . Thus

$$\begin{aligned} [p_A^A(x)] &= \frac{-2\alpha}{(1-M_\infty^2)^{1/2}} \frac{(1-x_c)^{1/2}}{x_c^{1/2}}, & 0 < x < x_c \\ &= \frac{-2\alpha}{(1-M_\infty^2)^{1/2}} \frac{(1-x)^{1/2}}{x^{1/2}}, & x_c \leq x \leq 1 \\ &= 0, & x > 1. \end{aligned} \quad (43)$$

The foregoing pressure jump distribution corresponds to that for a thin cambered airfoil which more closely resembles an inclined flat plate as  $x \rightarrow 1$ . The location of the airfoil camber line can be determined by integration after setting  $[p_D^A] = [p_A^A]$  and  $D_C = D_{C,A}$  in Eq. (11) and  $D_{C,A}(1) = 0$ .

Numerical results will be presented for symmetric ( $\alpha = 0$ ) and asymmetric, high-subsonic ( $M_\infty = 0.7$ ), turbulent flows at  $Re = 10^6$  to illustrate the effects of airfoil thickness and loading on the trailing-edge flow behaviour and separation phenomena. Qualitative comparisons between the results for low-subsonic ( $M_\infty = 0.1$ ) turbulent and laminar flows will also be given in the form of the mean flow streamlines. For all of these calculations the value of  $x_c$  was set at 0.75. Further, contributions to the pressures in the trailing-edge region from viscous displacement effects upstream ( $x < x_{IB} = 0.5$ ) and downstream ( $x > x_{IE} = 1.5$ ) of the strong-interaction solution domain have been regarded as negligible.

For the turbulent calculations the extent of the viscous solution domain normal to the airfoil was taken to extend to an  $\eta$  value of 11.0. This, together with the use of the scaling function  $g(x)$  in the definition of  $\xi$ , Eq. (13), places the outer boundary of the viscous-layer computational region sufficiently far from the body to properly calculate the entire viscous layer at all stream-wise locations. The distribution of points in the normal direction was chosen so

that the value of the parameter  $y^+ = yu_\tau/\mu$ , where  $y^+$  is a Reynolds number based on typical turbulent velocity and length scales, and  $u_\tau$  is the friction velocity (see Eq. 26d), was never greater than one at the first grid point off the surface. This is generally accepted as being sufficient to prevent the solution from being dependent on the normal grid spacing (e.g., see Ref. 23). A total of 41 grid points were used in the normal direction and stretching was applied to give the desired value of  $y^+$  at the first grid point. The same grid stretching was applied for the upper and lower surface boundary-layer calculations. In the wake 81 normal grid points were used. In addition, a total of 81 variably-spaced mesh lines were used in the streamwise direction with 51 points on the airfoil and 30 points in the wake. A minimum streamwise spacing,  $\Delta x_{\min}$ , of approximately .000259 was applied at the trailing edge. This is an order of magnitude smaller than the minimum spacing used in the laminar calculations of Ref. 2. The same streamwise distribution of points was used on both surfaces of the airfoil. The distribution of grid points used to calculate the laminar streamline contours illustrated in Figs. 8 and 9 was the same as that used in Ref. 2.

The interaction solution was globally iterated until the maximum relative change in the displacement thickness between two successive global iterations was less than  $1 \times 10^{-6}$ . This rather stringent level of convergence required about 50 iterations for a symmetric flow past a flat-plate trailing edge, and about 200 iterations for the most severe cases considered. Direct comparisons of the convergence rates obtained with the semi-inverse and quasi-simultaneous procedures were made for laminar flows and it was found that the rates achieved with the latter were from two to four times faster than those achieved with the former. Our turbulent flow calculations converged more slowly than those for corresponding laminar flow because a much finer grid was employed to resolve the flows in the vicinity of turbulent trailing edges. The mesh used here for the turbulent calculations was determined by the most severe case considered (i.e.,  $T = 0.06$ ,  $\alpha = 0$ ) for which a very short reverse-flow region was determined. For consistency the same mesh was then used for all of the turbulent calculations. However, a coarser mesh could be used for most of these cases and would result in more rapid convergence. The relaxation factor  $\omega$  was set to one, except for the turbulent symmetric flow with  $T = 0.06$ , where underrelaxation with  $\omega = 0.1$  was required to achieve a converged solution. Overrelaxation was not employed, but it probably could have been used to advantage for a number of the cases considered.

#### Symmetric Trailing-Edge Flows

Results illustrating the effect of airfoil thickness on the flow in the trailing-edge region are shown in Fig. 2. Values of  $T$  equal to 0 (flat-plate airfoil), 0.02, 0.04, and 0.06 have been considered. For a double-circular-arc trailing-edge profile ( $T > 0$ ) the viscous displacement thickness (Fig. 2a)

increases rapidly up to the trailing-edge point and then it decreases less rapidly along the wake. The net effect is a smoothing of the effective shape of the airfoil and its wake as seen by the outer inviscid flow. The skin friction coefficient,  $C_f$ , and wake centerline velocity distributions,  $u_w$ , shown in Fig. 2b indicate that the flow separates for  $T = 0.06$ . The skin friction coefficient and wake centerline velocity for  $T = 0.06$  is shown on an expanded scale in a region very close to the trailing edge in Fig. 2c. Note that in the separated-flow case there is an abrupt change in the skin friction coefficient just before the trailing edge. A similar behavior is seen in the separated laminar cases shown in Fig. 2b of Ref. 2. However, there it occurs over a considerably longer streamwise distance. In the turbulent calculation this feature could not be resolved without using an extremely fine grid at the trailing edge. First-order pressure ( $p$ ) distributions are shown in Fig. 2c. For the flat-plate airfoil the pressure decreases up to the trailing-edge point and then rapidly increases with increasing streamwise distance, rising to the freestream value ( $p_\infty = 0$ ) in the near wake. For the double-circular-arc trailing-edge configurations the pressure increases with  $x$  up to the trailing edge and into the near wake, and then it gradually drops towards its freestream value downstream. The flow separates only for  $T = 0.06$ , and the reverse-flow region is of very limited extent. In this case the pressure plateau typical of laminar trailing-edge separations is not evident; however, a more rounded peak in the pressure distribution is observed as  $T$  increases.

The differences in the flow behavior for the flat-plate and the thick airfoils can be explained as follows. The sudden removal of the no-slip condition at the trailing edge causes the flow to accelerate in the streamwise direction resulting in a thinning of the boundary layer, an increase in skin friction and a decrease in pressure as the trailing edge is approached. This behavior is illustrated by the flat-plate ( $T = 0$ ) results shown in Fig. 2. However, thick-airfoil closure (in a finite trailing-edge angle) causes the flow to decelerate as it approaches the trailing-edge point leading to a thickening of the boundary layer along with a decrease in skin friction and an increase in pressure. The turbulent results depicted in Fig. 2 and the laminar results shown in Fig. 2 of Ref. 2 reveal that even for the smallest thicknesses calculated, the decelerating effect due to thick airfoil closure is stronger than the accelerating effect due to the relief of the no-slip condition.

#### Asymmetric Trailing-Edge Flows

Asymmetric flow results will be presented for thin cambered airfoils with  $T = 0$  (Fig. 3) and for  $T = 0.02$  (Fig. 5). The camber distributions are defined by prescribing the loading parameter,  $\alpha$  in Eq. (43). The effects of viscous displacement and wake curvature on the pressure distributions acting on cambered flat-plate ( $T = 0$ ) and 2% thick airfoils with a loading parameter  $\alpha$  equal to 0.2

are depicted in Figs. 4 and 6, respectively. In addition, the effect of airfoil thickness is illustrated in Fig. 7 for a fixed value of the loading parameter equal to 0.05.

Results indicating the effect of loading on the turbulent mean flow in the vicinity of a cambered flat-plate airfoil operating at a Mach number of 0.7 and a Reynolds number of  $10^6$  (based on the airfoil chord) are shown in Fig. 3. Similar results have been reported in Ref. 1 for laminar flow at  $M_\infty = 0.1$ . The turbulent displacement thickness distributions are shown in Fig. 3a. The thickness of the suction-surface boundary layer increases while that of the pressure-surface boundary layer decreases with an increase in airfoil loading. The net effect is a thickening of the displacement body in the trailing-edge region with an increase in loading. These turbulent results show a very similar behavior to those obtained for laminar flow (at  $M_\infty = 0.1$ ) in Ref. 1, but the turbulent displacement thicknesses for  $M_\infty = 0.7$  are much larger than those for laminar flow at  $M_\infty = 0.1$ .

The skin friction coefficient and wake streamline velocity distributions are shown in Fig. 3b. For the symmetric case ( $\alpha = 0$ ) the skin friction increases on both sides of the airfoil as the flow accelerates approaching the trailing edge. However, for  $\alpha \neq 0$  the suction-surface skin friction coefficient generally decreases, except in the immediate vicinity of the trailing edge, and the pressure-surface coefficient increases with increasing distance along the airfoil. The acceleration of the flow before the trailing edge due to the relief of the no-slip boundary condition is evident in all of the pressure-surface results. However, on the suction surface and just before the trailing edge, the acceleration diminishes as the loading increases until at the higher loadings no local acceleration occurs. For  $\alpha \geq 0.2$  it appears that the decelerating effect of the adverse pressure gradient on the suction surface at the trailing edge is stronger than the local acceleration due to the relief of the no-slip boundary condition. There is very little effect of airfoil loading on the wake streamline velocity since the flows considered in Fig. 3 all remain attached to the airfoil surfaces. If a significant one-sided separation occurred as  $\alpha$  was increased, pronounced changes in the wake streamline velocity distribution would be observed (see Fig. 4 of Ref. 1). In addition, as expected, the turbulent mean flow accelerates much more rapidly along the wake to its free stream velocity than in a corresponding laminar flow.

The pressure distributions for the cambered flat-plate airfoil are shown in Fig. 3c. The increasing pressure difference across the airfoil with increasing  $\alpha$  can be seen, as well as the crossing of the pressure- and suction-surface pressures just upstream of the trailing edge leading to a small region of negative loading there. In the wake the pressure rises rapidly with increasing streamwise distance to its free stream value ( $p = 0$ ).

Although the contribution to the lift acting on the airfoil from the loading in the trailing-edge region increases with increasing  $\alpha$ , (Fig. 3c), viscous effects cause a significant reduction in the lift that would be predicted from inviscid considerations alone. The thickening and thinning of the suction- and pressure-surface boundary layers, respectively, with increasing loading tend to uncamber the airfoil. In general, both displacement and wake curvature effects tend to decrease the loading on the airfoil, but for turbulent flow at a Reynolds number of  $10^6$  around a cambered flat plate the effect of wake curvature is generally much smaller than that of viscous displacement. This is evident from the results presented in Fig. 4 for  $\alpha = 0.2$ . Here the inviscid pressure distribution over the airfoil is shown along with the pressure that results when viscous displacement effects are included, and finally, when viscous displacement and wake curvature effects are included. The wake curvature effect tends to decrease the loading on the airfoil over that due to viscous displacement alone, giving rise to a negative loading in the immediate vicinity of the trailing edge.

The effects of loading on a two-percent thick airfoil are considered in Fig. 5. A comparison of these results with those for the zero-thickness airfoil (Fig. 3) reveals a significant effect of airfoil thickness on the asymmetric flow behaviour in the trailing-edge region. In particular, the displacement thickness (Fig. 5a) tends to increase on both the pressure- and suction-surfaces of the finite-thickness airfoil as the trailing edge is approached. In contrast, for the cambered flat-plate airfoil, the displacement thickness decreases with distance along the pressure surface just upstream of the trailing edge. This difference in behaviour is due to the decelerating effect of thick airfoil closure.

The skin friction coefficient and wake streamline velocity distributions are depicted in Fig. 5b. Airfoil thickness causes the skin friction coefficient to decrease on both the suction and pressure surfaces of the airfoil as the trailing edge is approached. The flows considered in Fig. 5 remain attached to the airfoil surfaces, but the results suggest that separation will occur on the suction surface for sufficiently large values of the loading parameter,  $\alpha$ .

The pressure distributions for the two-percent thick loaded airfoils are shown in Fig. 5c. Again, the surface pressures for the two-percent thick airfoil behave quite differently than those for the cambered flat-plate airfoil (Fig. 3c). For the latter, the suction- and pressure-surface pressures tend to increase and decrease, respectively, with distance along the airfoil. At the trailing-edge point the pressure is below its free stream value ( $p = 0$ ) and then

it rises rapidly to  $p = 0$  in the near wake. For the thick airfoils (Fig. 5c) the pressures on both airfoil surfaces near the trailing edge (say for  $x > .85$ ) are generally lower than those for the corresponding zero-thickness airfoils, but they rise rapidly to a level, at the trailing edge, which is greater than the free-stream pressure. In the near wake the pressure drops back to the free-stream level at a relatively slow rate.

The effects of the viscous displacement and wake curvature upon the pressure distributions for the cambered flat-plate (Fig. 4) and the two-percent thick (Fig. 6) airfoils are similar. However, the effect of wake curvature on the pressure distribution for the two-percent thick airfoil (Fig. 6) is considerably smaller than that indicated in Fig. 4 for the cambered flat plate airfoil.

The effect of varying airfoil thickness for a fixed value of the loading parameter,  $\alpha$ , is illustrated in Fig. 7. The value of  $\alpha$  for which these calculations were performed is 0.05, and the values of the thickness parameter,  $T$ , are 0, 0.02, 0.04. We have not been able to determine a turbulent solution for  $T = 0.06$  because of difficulties in converging the calculation caused by large displacement thicknesses and the use of small grid spacings to resolve the flow in the vicinity of the trailing edge.

The displacement thicknesses on both surfaces become larger at the trailing edge as the airfoil thickness increases (Fig. 7a). However, the difference between the upper- and lower-surface displacement thicknesses does not change significantly, compared with the change in the displacement thickness itself. For the thick airfoils the skin friction coefficient decreases along both surfaces as the trailing edge is approached (Fig. 7b), with the flow on the suction surface of the four-percent thick airfoil being close to separation at the trailing edge. Another effect of increasing the airfoil thickness is to retard the approach of the wake streamline velocity to the free-stream value. Finally, the pressure distributions are shown in Fig. 7c. For the attached flows around the 2% and 4% thick airfoils the pressure reaches a maximum value just aft of the trailing edge, and this value increases with increasing thickness. Also, the loading on the airfoil near the trailing edge decreases as the airfoil thickness increases. In fact, for  $T = 0.04$ , there is almost no loading over approximately the last 5% of airfoil chord. Finally, the distance along the wake required for the pressure to return to its free stream value increases with increasing thickness.

#### Streamlines for Laminar and Turbulent Mean Flows

It is helpful in attempting to understand the behaviour of the flow in the trailing-edge region to examine streamline contours. Values of the stream function in the viscous layer,  $\psi(x, \tilde{y})$ , are determined from the relation

$$\psi = \int_0^{\tilde{y}} \rho u d\tilde{y} = \sqrt{2\xi} \int_0^{\eta} F d\eta \quad (44)$$

where  $\psi$  is taken to be zero on the surfaces of the airfoil and on the reference wake streamline; i.e., at  $\tilde{y} = 0$ . After evaluating  $\psi$  at the mesh points used in the viscous-layer calculation, a standard contour plotting package has been applied to map lines of constant  $\psi$  and to produce the streamline plots shown in Figs. 8 and 9. In these figures the same contour levels for  $\psi$  are displayed. The Mach number  $M_\infty$  for the cases presented in Figs. 8 and 9 is 0.1. The calculations were performed at this Mach number because of difficulties in converging the laminar flow calculations at the Mach number,  $M_\infty = 0.7$ , used in the previous examples. This is due to the fact that an increase in Mach number tends to increase the severity of the viscid/inviscid interaction (see Ref. 1), which in turn leads to difficulties in obtaining a converged solution.

In Fig. 8 the streamline patterns for laminar and turbulent mean flows are illustrated for the symmetric flow over a two-percent thick airfoil. The laminar flow (Fig. 8a) is seen to have an extensive separation bubble, with the reverse-flow region extending over approximately 25% of airfoil chord. The corresponding turbulent flow (Fig. 8b) is fully attached. In Fig. 9 the laminar and turbulent mean flow streamlines are depicted for asymmetric flow ( $\alpha = 0.07$ ) over a one-percent thick airfoil. The laminar case (Fig. 9a) has a rather extensive region of one-sided separation. On the other hand, the turbulent flow (Fig. 9b) remains fully attached to the airfoil. These figures dramatically illustrate the effect that turbulence can have on suppressing a separation of the viscous layer at the trailing edge of a thick and/or loaded airfoil.

## CONCLUDING REMARKS

An analytical procedure based on finite Reynolds number interacting boundary-layer theory has been developed for predicting subsonic turbulent mean flow in the trailing-edge and near-wake region of an airfoil. A quasi-simultaneous coupling procedure, which is characterized by a local coupling of the viscous and inviscid solutions at each iteration level, is utilized, within an overall global iteration strategy, to provide a relatively efficient solution technique for flows with strong viscous/inviscid interactions. We find that the superposition procedure used to determine inverse viscous-layer solutions leads to a relatively simple implementation of the quasi-simultaneous coupling procedure for asymmetric wakes. This analysis will provide a useful basis for future studies on turbulent mean-flow behavior, including separation phenomena, in the vicinity of an airfoil trailing edge. In particular it will allow detailed investigations to be made on the effects of airfoil geometry, turbulence behavior and oncoming boundary layer profiles on the mean flow in the trailing-edge/near-wake region of an airfoil.

Numerical results have been presented for symmetric and asymmetric mean flows past a prescribed family of airfoil trailing edges. The behavior of the flow in the airfoil trailing-edge and near-wake region, as the parameters governing the airfoil thickness and camber distributions are varied, has been demonstrated through a systematic parametric study. The effect of wake curvature on the airfoil and near-wake pressure distribution is found to be much smaller than the effect of viscous displacement for the airfoil geometries and free stream Mach and Reynolds numbers considered here. Both effects tend to uncamber the airfoil, leading to a reduction in the lift predicted by a purely inviscid analysis. Separation at the trailing edge of a symmetric configuration is observed to occur for a significantly thicker airfoil when the flow is turbulent than when it is laminar. In addition, whereas in earlier laminar-flow studies (Refs. 1 and 2) one-sided separation was observed, it was not predicted in the present turbulent investigation. Because significantly more severe geometries than those which induce laminar separation are required to cause a turbulent mean flow to separate, and the use of linearized inviscid theory limits the severity of the configurations that can be analyzed, a fully nonlinear inviscid flow representation should be considered in future work to permit consideration of highly-loaded airfoils.

During the course of this investigation a small symmetric turbulent separation was predicted at the trailing edge of a six-percent thick airfoil. Very small grid spacings in the streamwise direction were applied to obtain this solution. Unfortunately, this requirement tends to decrease the convergence rate of the global viscous/inviscid iteration procedure. Although the resultant low convergence rate could be accepted for obtaining benchmark solutions such as

those calculated herein, additional work is required to make the present procedure a more efficient one for practical calculations of strong viscid/inviscid trailing-edge interactions. Another area for possible future consideration is the development of methods incorporating wake curvature effects into the strong-interaction solution procedure to permit the accurate prediction of flow past highly loaded airfoils for which such effects could be significant. This would entail the inclusion of normal pressure gradients in the viscous-layer formulation, and may have a strong impact on turbulent mean-flow solutions in the vicinity of a highly loaded airfoil trailing edge. In addition, alternative turbulence models better capable of representing separated flows than the algebraic eddy viscosity model used in this investigation, must be considered in order to improve the predictive capability of a viscid/inviscid interaction analysis.

## REFERENCES

1. Vatsa, V. N. and Verdon, J. M., "Viscous/Inviscid Interaction Analysis of Asymmetric Trailing-Edge Flows," Numerical and Physical Aspects of Aerodynamic Flows, Edited by T. Cebeci, Springer-Verlag, New York, 1984, pp. 205-221.
2. Vatsa, V. N. and Verdon, J. M., "Viscid/Inviscid Interaction Analysis of Separated Trailing-Edge Flows," AIAA Journal, Vol. 23, April 1985, pp. 481-489.
3. Smith, F. T., "Interacting Flow Theory and Trailing-Edge Separation - No Stall," Journal of Fluid Mechanics, Vol. 131, June 1983, pp. 219-250.
4. Smith, F. T., "On the High Reynolds Number Theory of Laminar Flows," IMA Journal of Applied Mathematics, Vol. 28, May 1982, pp. 207-281.
5. Elliott, J. W. and Smith, F. T., "Separated Supersonic Flow Past a Trailing Edge at Incidence," to appear in Computers and Fluids, 1985.
6. Veldman, A. E. P. "The Calculation of Incompressible Boundary Layers with Strong Viscous-Inviscid Interaction," AGARD Symposium on Computation of Viscous-Inviscid Flows, AGARD-CPP-291, 1980, Chapter 12.
7. Veldman, A. E. P. and Lindhout, J. P. F., "Quasi-Simultaneous Calculations of Strongly Interacting Viscous Flow," presented at the Third Symposium on Numerical and Physical Aspects of Aerodynamic Flows," Long Beach, California, Jan. 21-24, 1985.
8. Cebeci, T. and Smith, A. M. O., Analysis of Turbulent Boundary Layers, Academic Press, New York, 1974, pp. 211-239.
9. Cebeci, T., Thiele, F., Williams, P. G. and Stewartson, K., "On the Calculation of Symmetric Wakes I. Two-Dimensional Flows," Numerical Heat Transfer, Vol. 2, 1979, pp. 35-60.
10. Brown, S. N. and Stewartson, K., "Wake Curvature and the Kutta Condition in Laminar Flow," The Aeronautical Quarterly, Vol. 26, 1975, pp. 275-280.
11. Ashley, H. and Landahl, M., Aerodynamics of Wings and Bodies, Addison-Wesley Publishing Company, Inc., Reading, Massachusetts, 1965, pp. 88-97.

## REFERENCES (Cont'd)

12. Davis, R. T. and Werle, M. J., "Progress on Interacting Boundary-Layer Computations at High Reynolds Number," Numerical and Physical Aspects of Aerodynamic Flows, Springer-Verlag, 1982, pp. 187-210.
13. Vatsa, V. N., Werle, M. J. and Verdon, J. M., "Viscid/Inviscid Interaction at Laminar and Turbulent Symmetric Trailing Edges," AIAA Paper No. 82-0165, Orlando, Florida, Jan. 11-14, 1982.
14. Carter, J. E. and Wornom, S. F., "Solutions for Incompressible Separated Boundary Layers Including Viscid-Inviscid Interaction," in Aerodynamic Analyses Requiring Advanced Computers, Part I, prepared by NASA Langley Research Center, March 1975, pp. 125-150.
15. Cebeci, T., Clark, R. W., Chang, K. C., Halsey, N. D. and Lee, K., "Airfoils with Separation and the Resulting Wakes," presented at the Third Symposium on Numerical and Physical Aspects of Aerodynamic Flows," pp. 2-13 - 2-25, January, 1985.
16. Carter, J. E., "A New Boundary Layer Interaction Technique for Separated Flows," AIAA Paper No. 79-1450, Williamsburg, Virginia, July 23-24, 1979.
17. Wigton, I. B. and Hoyt, M., "Viscous-Inviscid Interaction in Transonic Flow," AIAA Paper 81-1003, Palo Alto, California, June 1982.
18. Edwards, D. E., and Carter, J. E., "A Quasi-Simultaneous Finite Difference Approach for Strongly Interacting Flow," presented at the Third Symposium on Numerical and Physical Aspects of Aerodynamic Flows, January, 1985, pp. 1-63 - 1-73.
19. Veldman, A. E. P., "New, Quasi-Simultaneous Method to Calculate Interacting Boundary Layers," AIAA Journal, Vol. 19, Jan. 1981, pp. 79-85.
20. Davis, R. T., "A Procedure for Solving the Compressible Interacting Boundary Layer Equations for Subsonic and Supersonic Flows," AIAA Paper No. 84-1614, Snowmass, Colorado, June 25-27, 1984.
21. Le Balleur, J. C. and Girodroux-Lavigne, P., "A Semi-Implicit and Unsteady Numerical Method of Viscous-Inviscid Interaction for Transonic Separated Flows," La Recherche Aerospaciale, No. 1984-1.
22. Reyhner, T. A. and Flügge-Lotz, I., "The Interaction of a Shock Wave with a Laminar Boundary Layer," International Journal on Nonlinear Mechanics, Vol. 3, No. 2, pp. 173-179.

REFERENCES (Cont'd)

23. Horstman, C. C., "Prediction of Separated Asymmetric Trailing-Edge Flows at Transonic Mach Numbers," AIAA Journal, Vol. 21, September 1983, pp. 1255-1261.

## LIST OF FIGURES

1. High Reynolds number flow around a thin airfoil.
2. Symmetric trailing-edge flow: effect of airfoil thickness;  $M_\infty = 0.7$ ,  $Re = 10^6$ ,  $\alpha = 0$ :
  - a) Displacement thickness distributions.
  - b) Skin friction and wake centerline velocity distributions.
  - c) Pressure distributions.
3. Asymmetric trailing-edge flow: effect of airfoil loading;  $M_\infty = 0.7$ ,  $Re = 10^6$ ,  $T = 0$ :
  - a) Displacement thickness distributions.
  - b) Skin friction and wake streamline velocity distributions.
  - c) Pressure distributions.
4. Viscous effects on the pressure in the trailing-edge region of a cambered flat-plate airfoil;  $M_\infty = 0.7$ ,  $Re = 10^6$ ,  $\alpha = 0.2$ ,  $T = 0$ . ----- Airfoil; — — — Airfoil + viscous displacement; ——— Airfoil + viscous displacement + wake curvature.
5. Asymmetric trailing-edge flow: effect of airfoil loading for a 2% thick airfoil;  $M_\infty = 0.7$ ,  $Re = 10^6$ ,  $T = 0.02$ :
  - a) Displacement thickness distributions.
  - b) Skin friction and wake streamline velocity distributions.
  - c) Pressure distributions.
6. Viscous effects on the pressure in the trailing-edge region of a 2% thick airfoil;  $M_\infty = 0.7$ ,  $Re = 10^6$ ,  $\alpha = 0.2$ ,  $T = 0.02$ . ----- Airfoil, — — — Airfoil + viscous displacement; ——— Airfoil + viscous displacement + wake curvature.

## LIST OF FIGURES (Cont'd)

7. Asymmetric trailing-edge flow: effect of airfoil thickness;  $M_\infty = 0.7$ ,  $Re = 10^6$ ,  $\alpha = 0.05$ :
  - a) Displacement thickness distributions.
  - b) Skin friction and wake streamline velocity distributions.
  - c) Pressure distributions.
8. Effect of turbulence on trailing-edge streamline pattern for symmetric flow with  $M_\infty = 0.1$ ,  $Re = 10^6$ ,  $\alpha = 0$  and  $T = 0.02$ : (a) laminar flow (b) turbulent flow.
9. Effect of turbulence on trailing-edge streamline pattern for asymmetric flow with  $M_\infty = 0.1$ ,  $Re = 10^6$ ,  $\alpha = 0.07$  and  $T = 0.01$ : (a) laminar flow (b) turbulent flow.



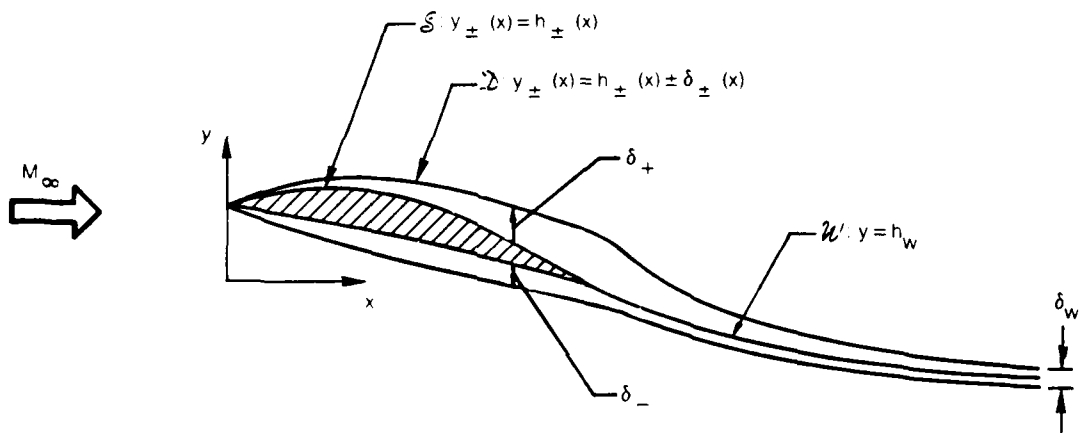
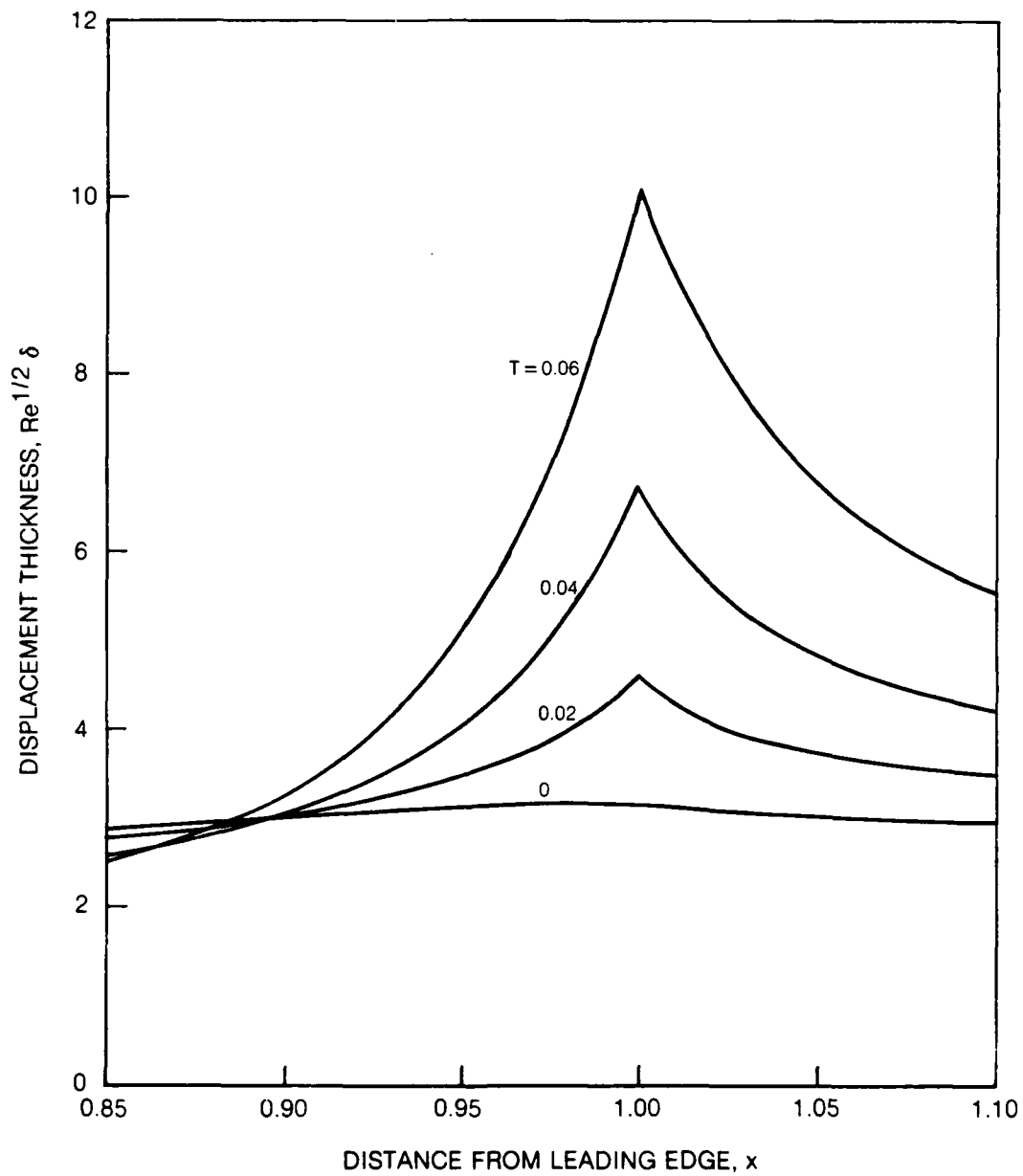
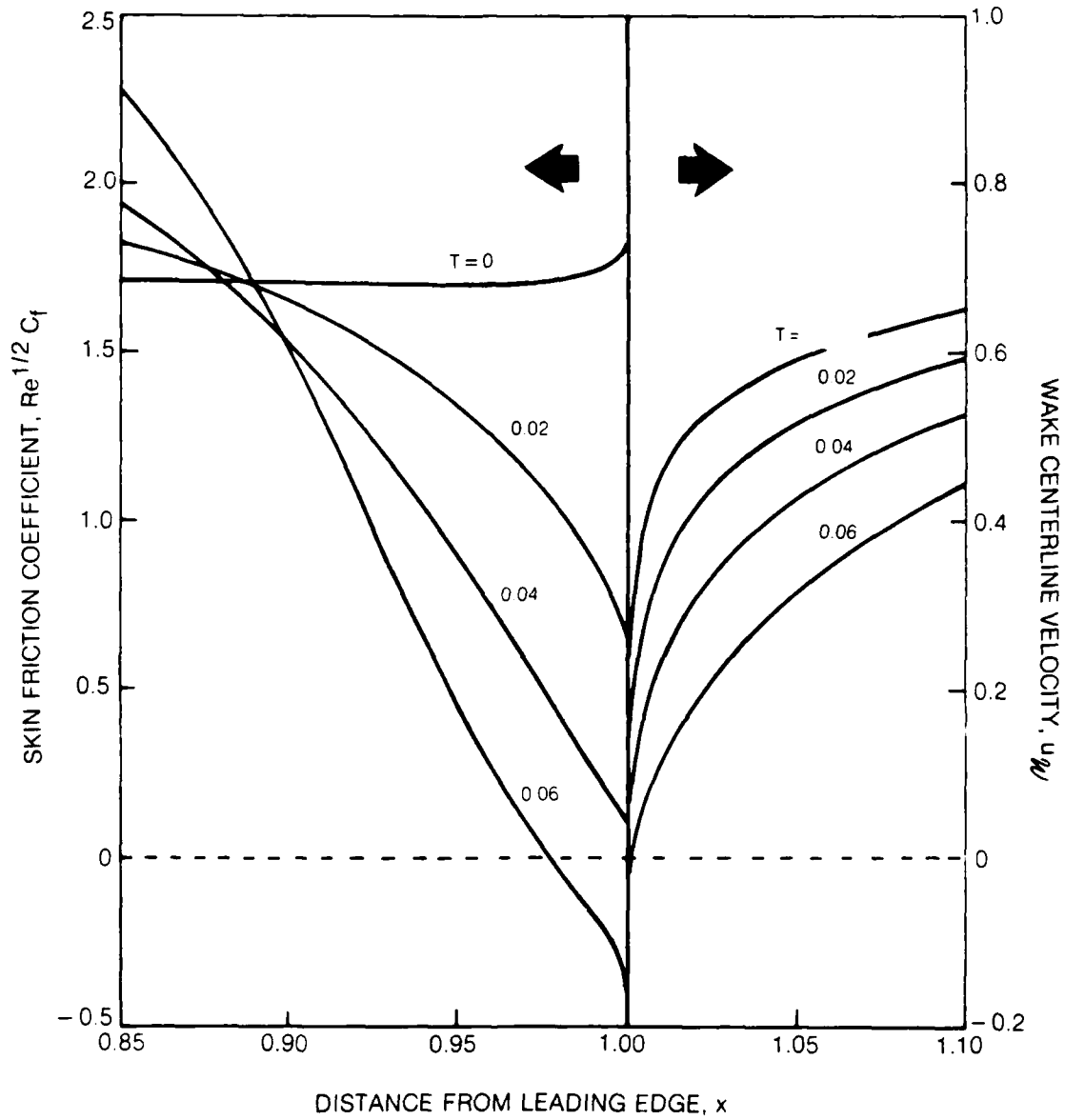


Fig. 1 High Reynolds number flow around a thin airfoil.



**Fig. 2 Symmetric trailing-edge flow: effect of airfoil thickness;  $M_\infty = 0.7$ ,  $Re = 10^6$ ,  $\alpha = 0$ : a) Displacement thickness distributions.**



**Fig. 2 Symmetric trailing-edge flow: effect of airfoil thickness;  $M_\infty = 0.7$ ,  $Re = 10^6$ ,  $\alpha = 0$ : b) Skin friction and wake centerline velocity distributions.**

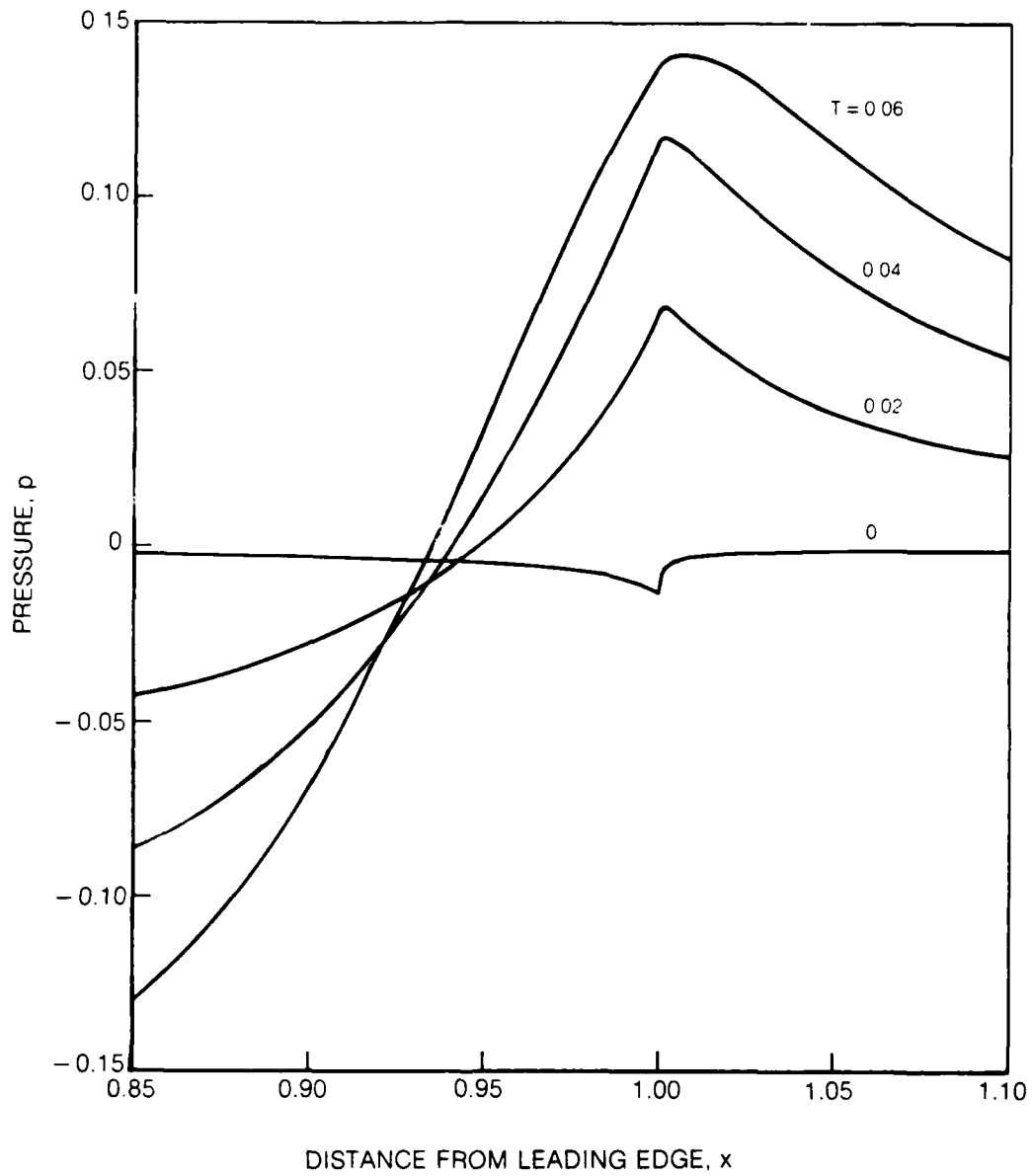


**Fig. 2 Symmetric trailing-edge flow: effect of airfoil thickness;  $M_\infty = 0.7$ ,  $Re = 10^6$ ,  $\alpha = 0$ : c) Pressure distributions.**

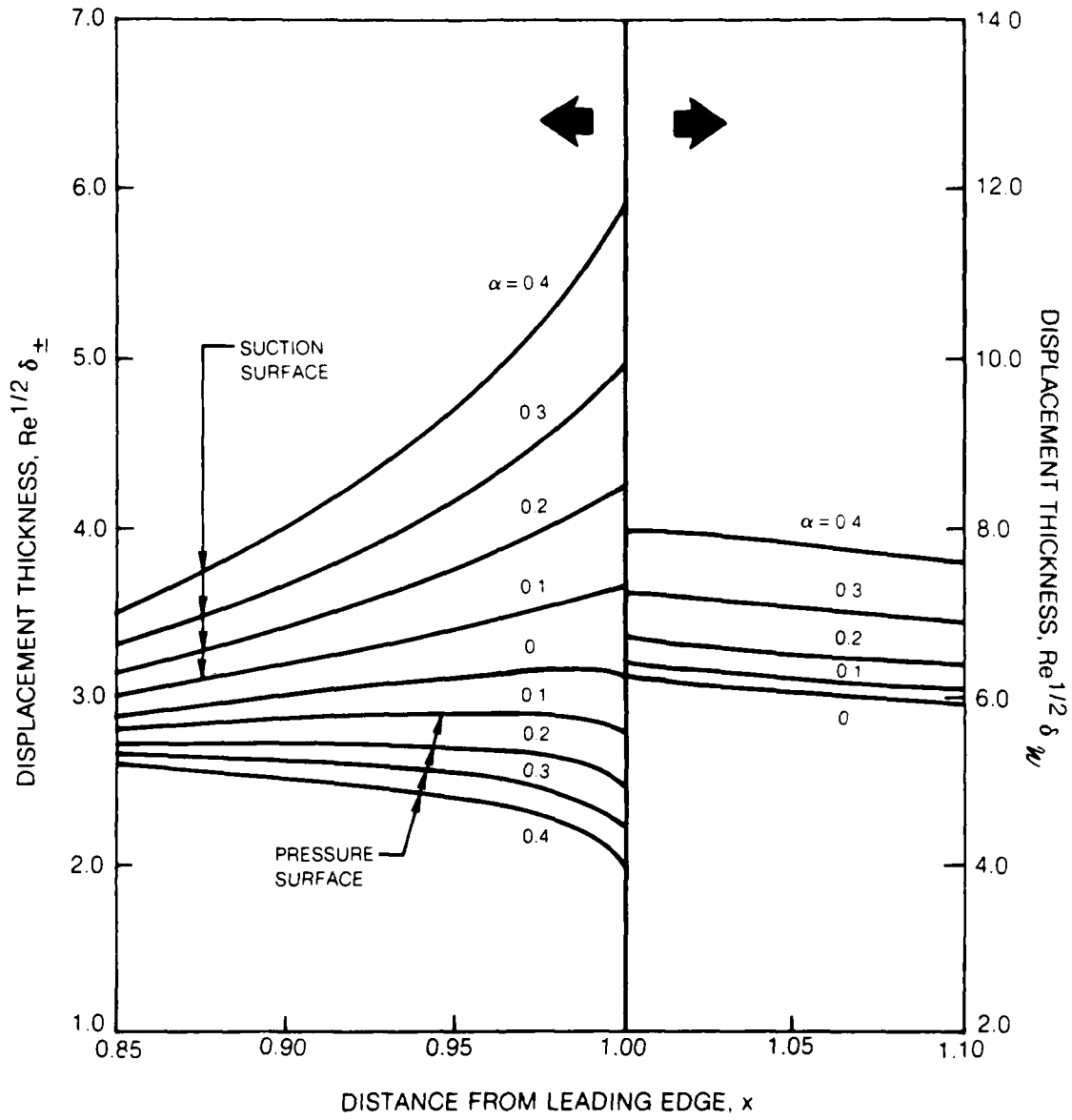


**Fig. 3 Asymmetric trailing-edge flow: effect of airfoil loading;**  
 $M_{\infty} = 0.7, Re = 10^6, T = 0$ : a) Displacement thickness distributions.

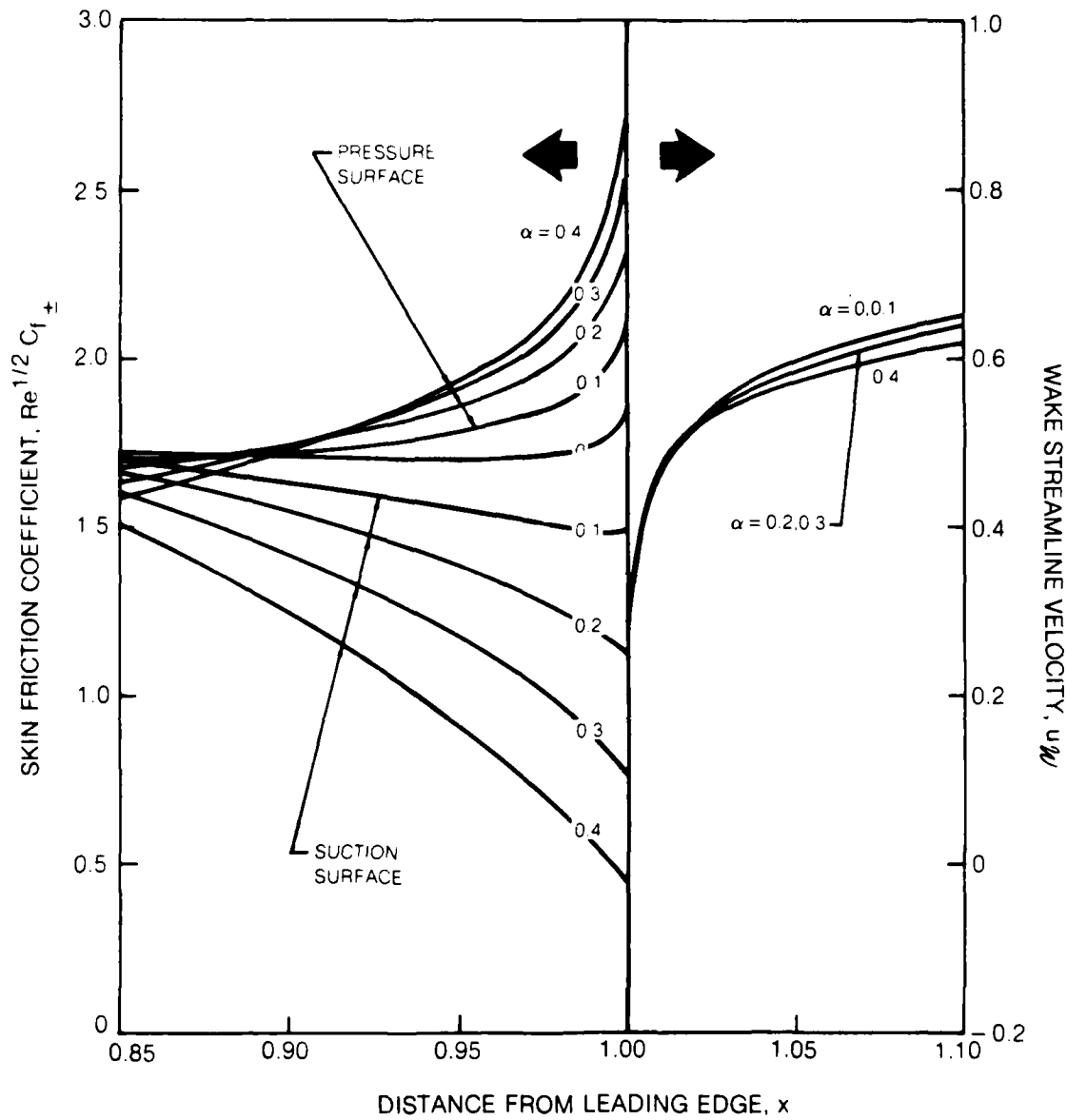


**Fig. 3 Asymmetric trailing-edge flow: effect of airfoil loading;  $M_\infty = 0.7$ ,  $Re = 10^6$ ,  $T = 0$ : b) Skin friction and wake streamline velocity distributions.**

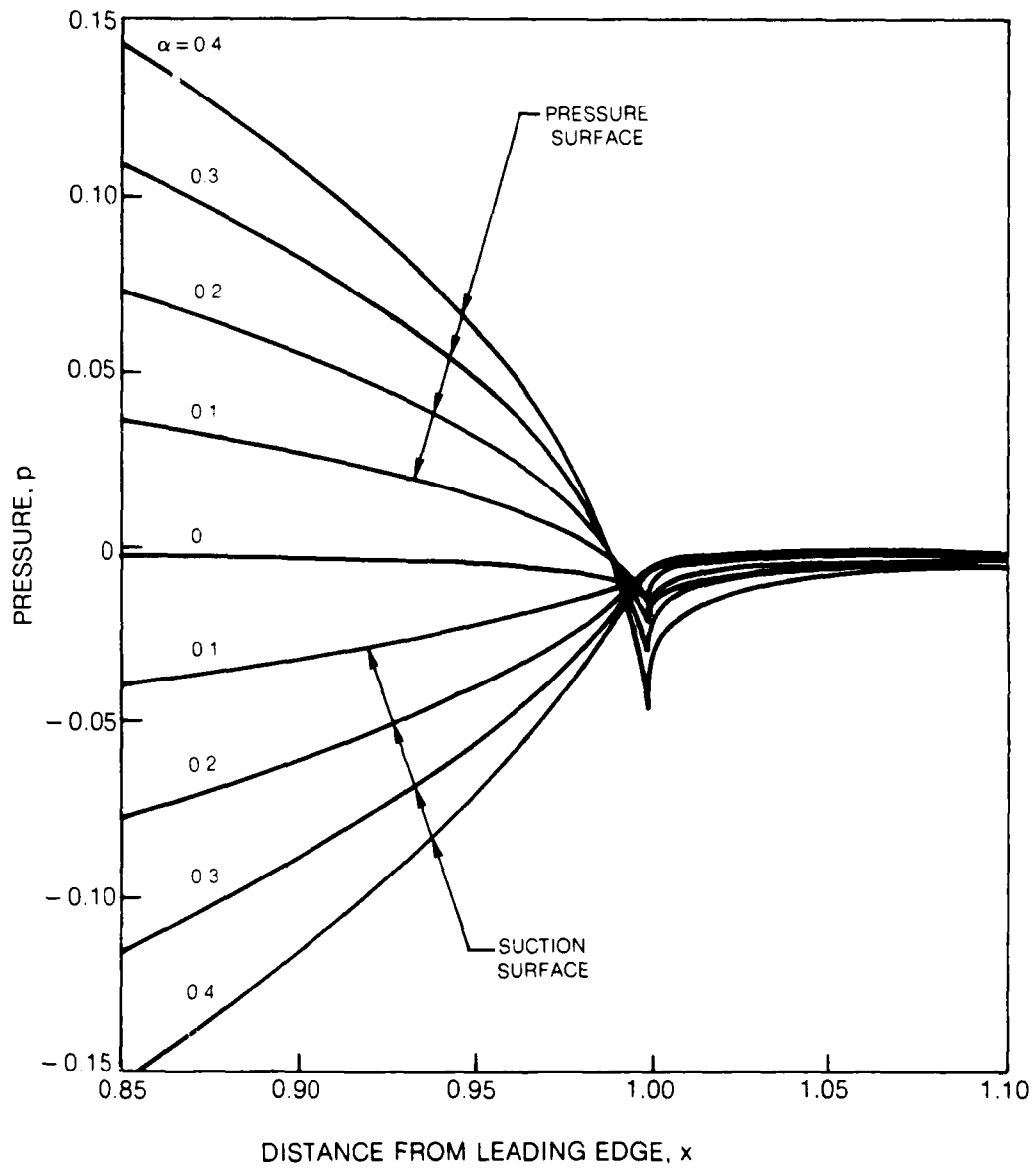


**Fig. 3 Asymmetric trailing-edge flow: effect of airfoil loading;  $M_\infty = 0.7$ ,  $Re = 10^6$ ,  $T = 0$ : c) Pressure distributions.**

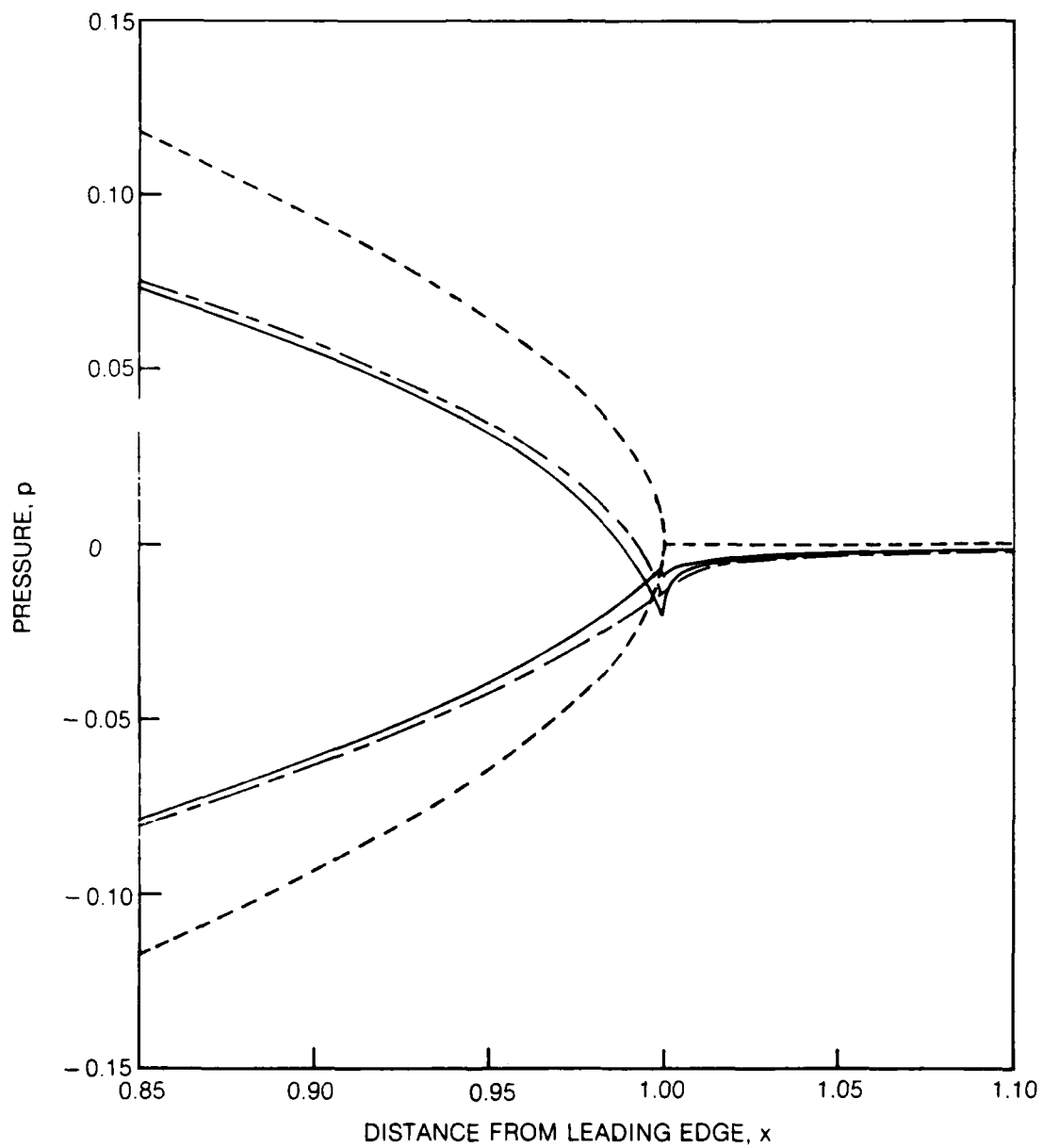


**Fig. 4 Viscous effects on the pressure in the trailing-edge region of a cambered flat-plate airfoil;  $M_\infty = 0.7$ ,  $Re = 10^6$ ,  $\alpha = 0.2$ ,  $T = 0$ .**  
 - - - - Airfoil; — · — Airfoil + viscous displacement;  
 — Airfoil + viscous displacement + wake curvature.

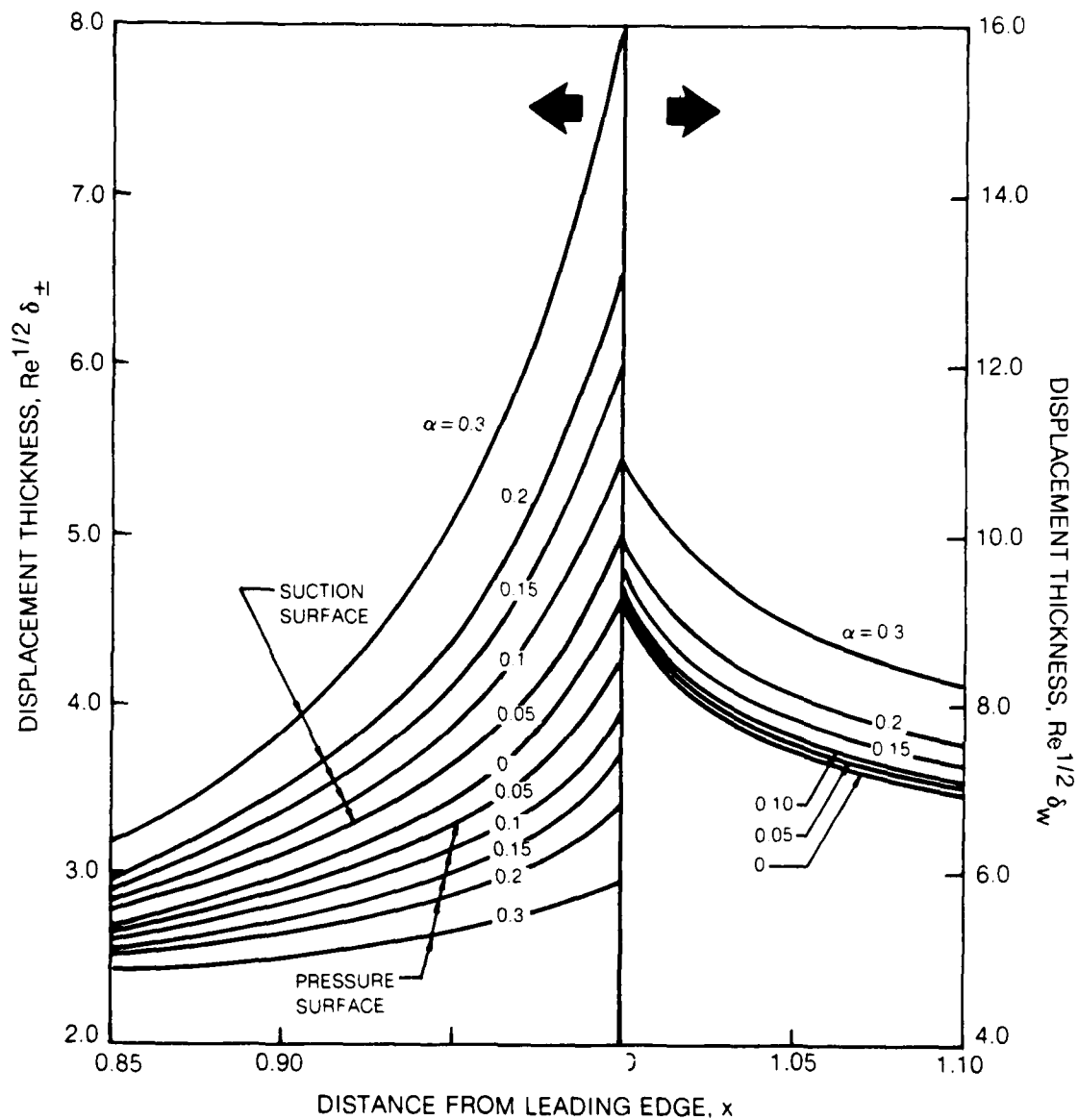


**Fig. 5 Asymmetric trailing-edge flow: effect of airfoil loading for a 2% thick airfoil;  $M_{\infty} = 0.7$ ,  $Re = 10^6$ ,  $T = 0.02$ : a) Displacement thickness distributions.**

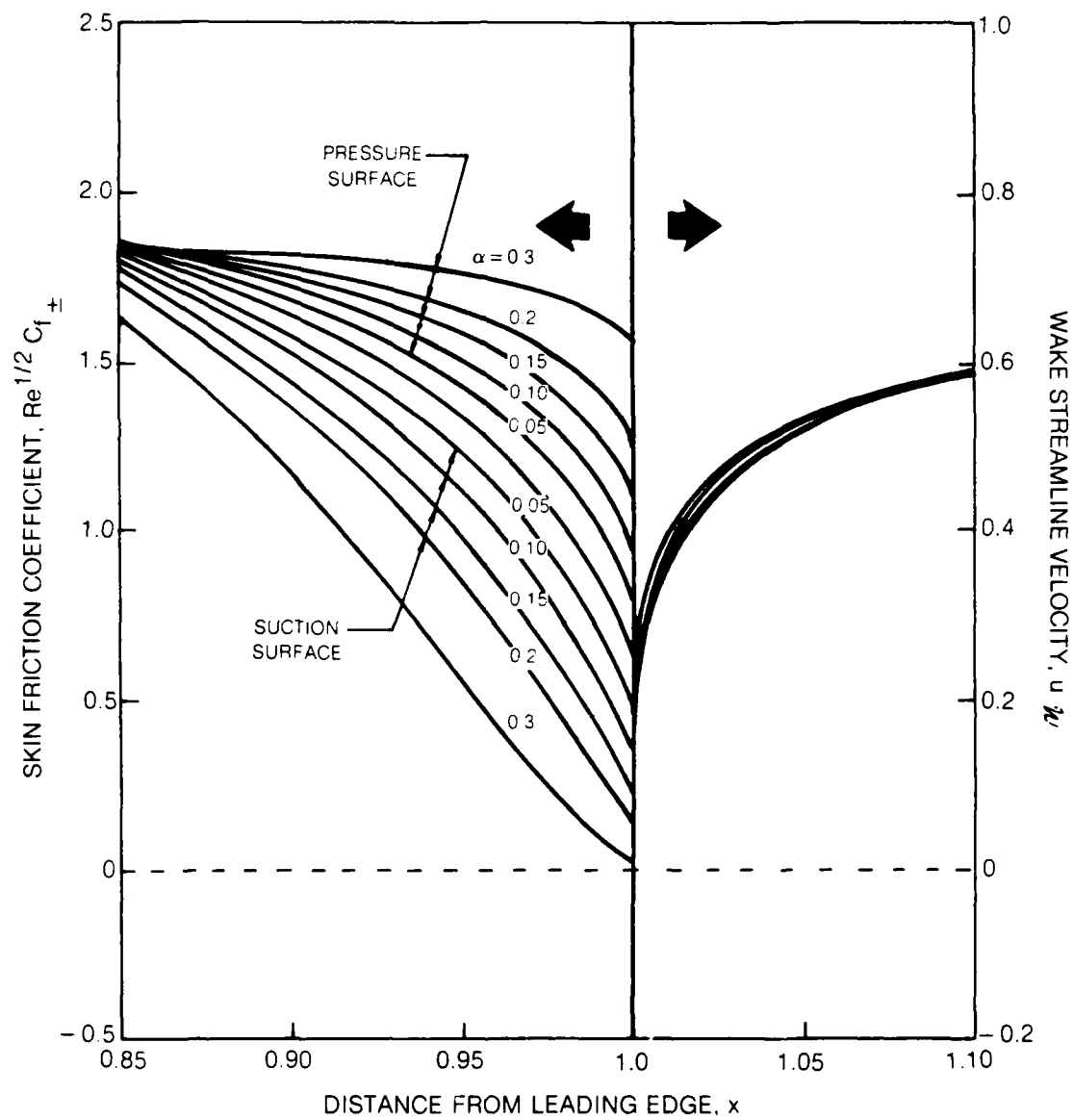


**Fig. 5 Asymmetric trailing-edge flow: effect of airfoil loading for a 2% thick airfoil;  $M_{\infty} = 0.7$ ,  $Re = 10^6$ ,  $T = 0.02$ : b) Skin friction and wake streamline velocity distributions.**

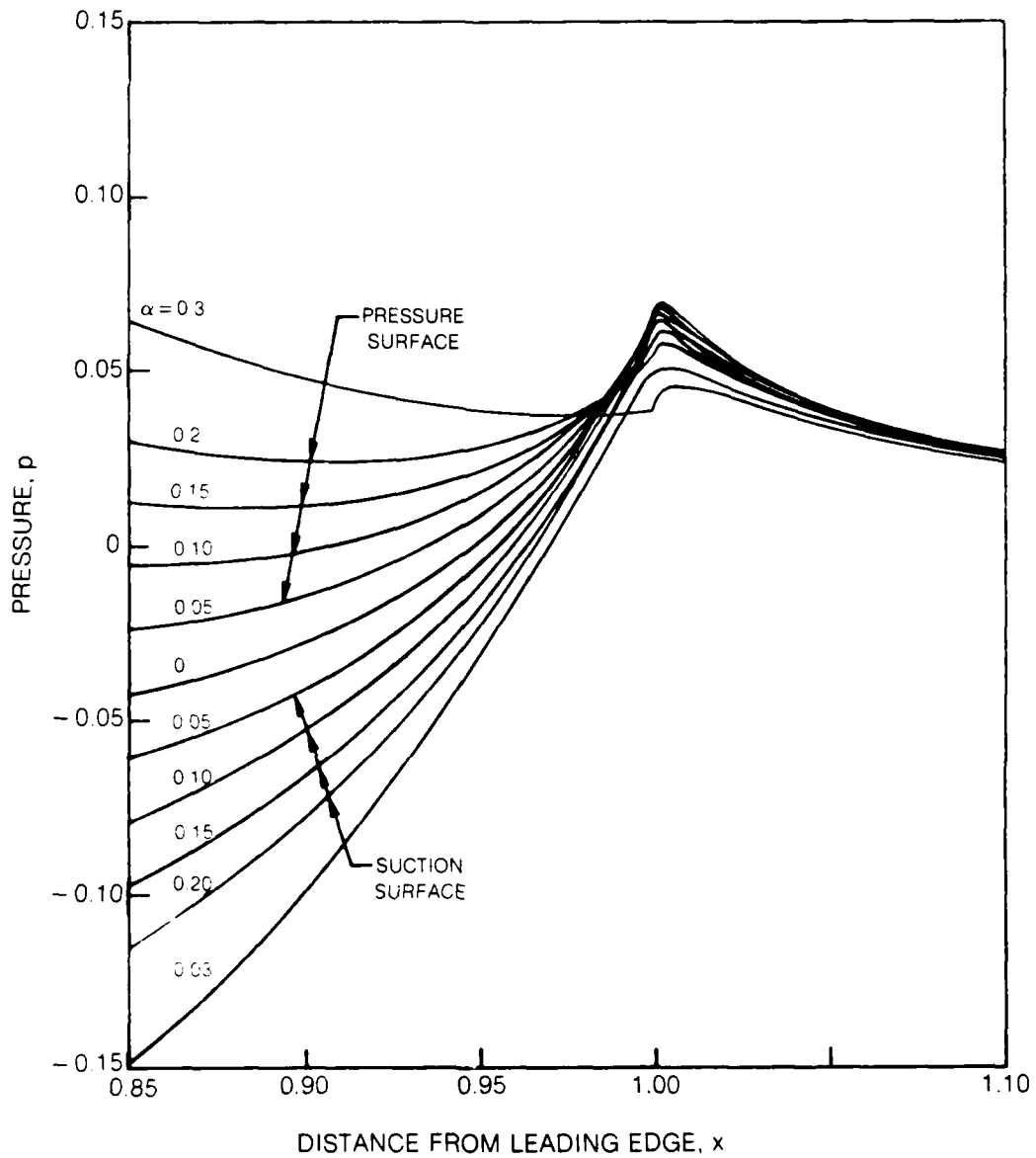


**Fig. 5 Asymmetric trailing-edge flow: effect of airfoil loading for a 2% thick airfoil;  $M_\infty = 0.7$ ,  $Re = 10^6$ ,  $T = 0.02$ : c) Pressure distributions.**

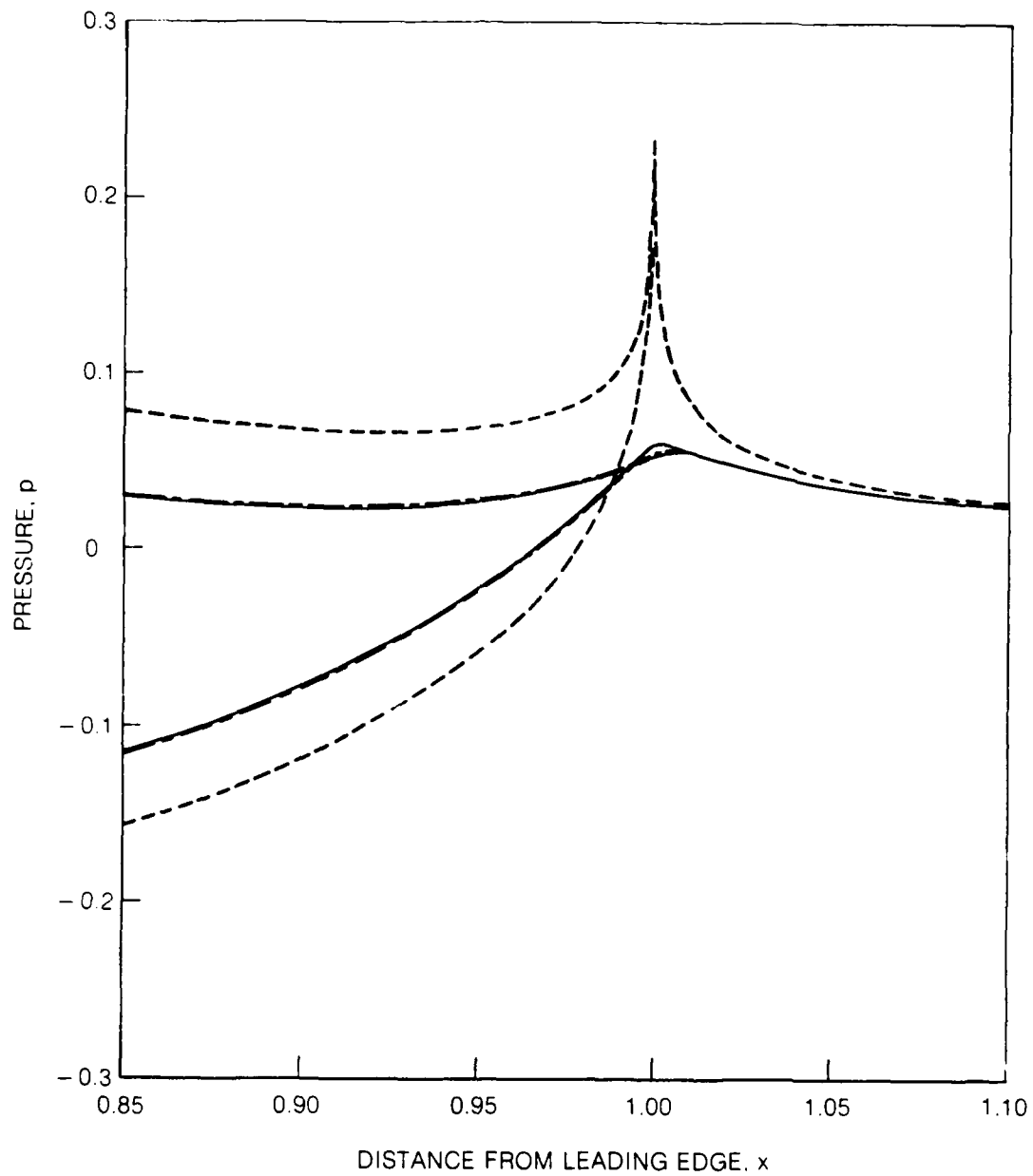


**Fig. 6** Viscous effects on the pressure in the trailing-edge region of a 2% thick cambered airfoil;  $M_\infty = 0.7$ ,  $Re = 10^6$ ,  $\alpha = 0.2$ ,  $T = 0.02$ . - - - - Airfoil; — — — Airfoil + viscous displacement; — — — Airfoil + viscous displacement + wake curvature.

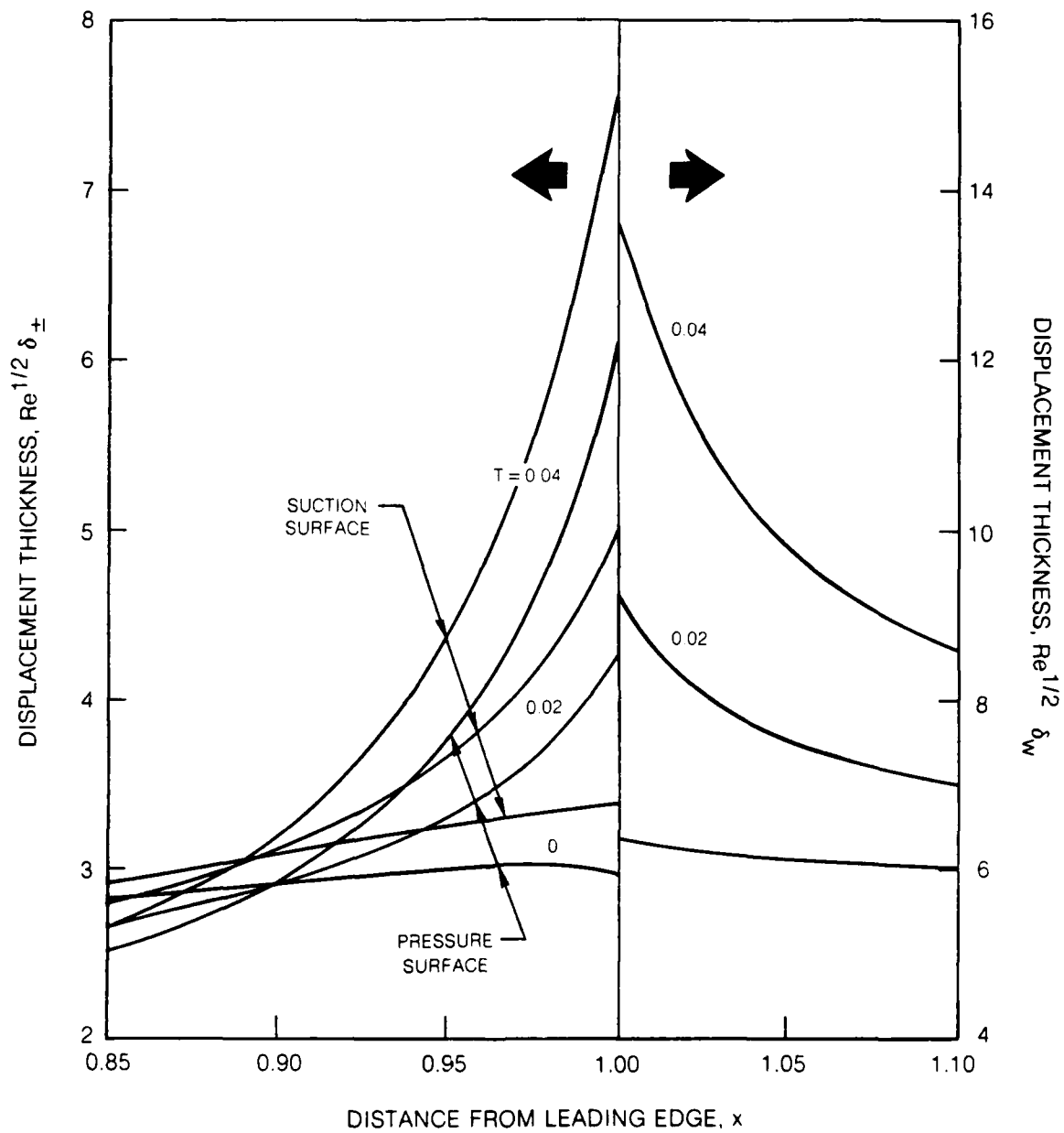


**Fig. 7 Asymmetric trailing-edge flow: effect of airfoil thickness;**  
 $M_{\infty} = 0.7$ ,  $Re = 10^6$ ,  $\alpha = 0.05$ : a) Displacement thickness distributions.

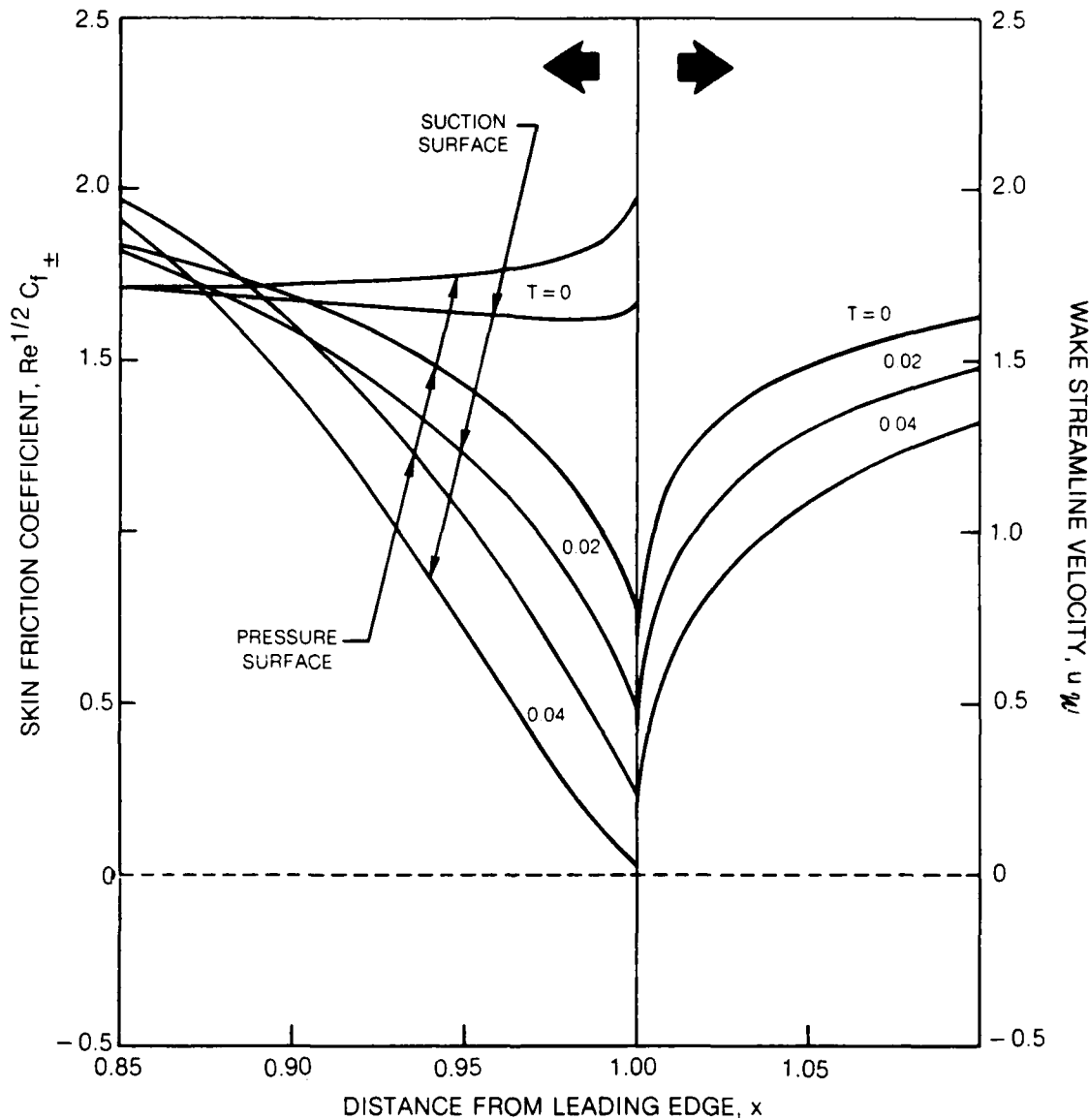


**Fig. 7 Asymmetric trailing-edge flow: effect of airfoil thickness;  $M_\infty = 0.7$ ,  $Re = 10^6$ ,  $\alpha = 0.05$ : b) Skin friction and wake streamline velocity distributions.**

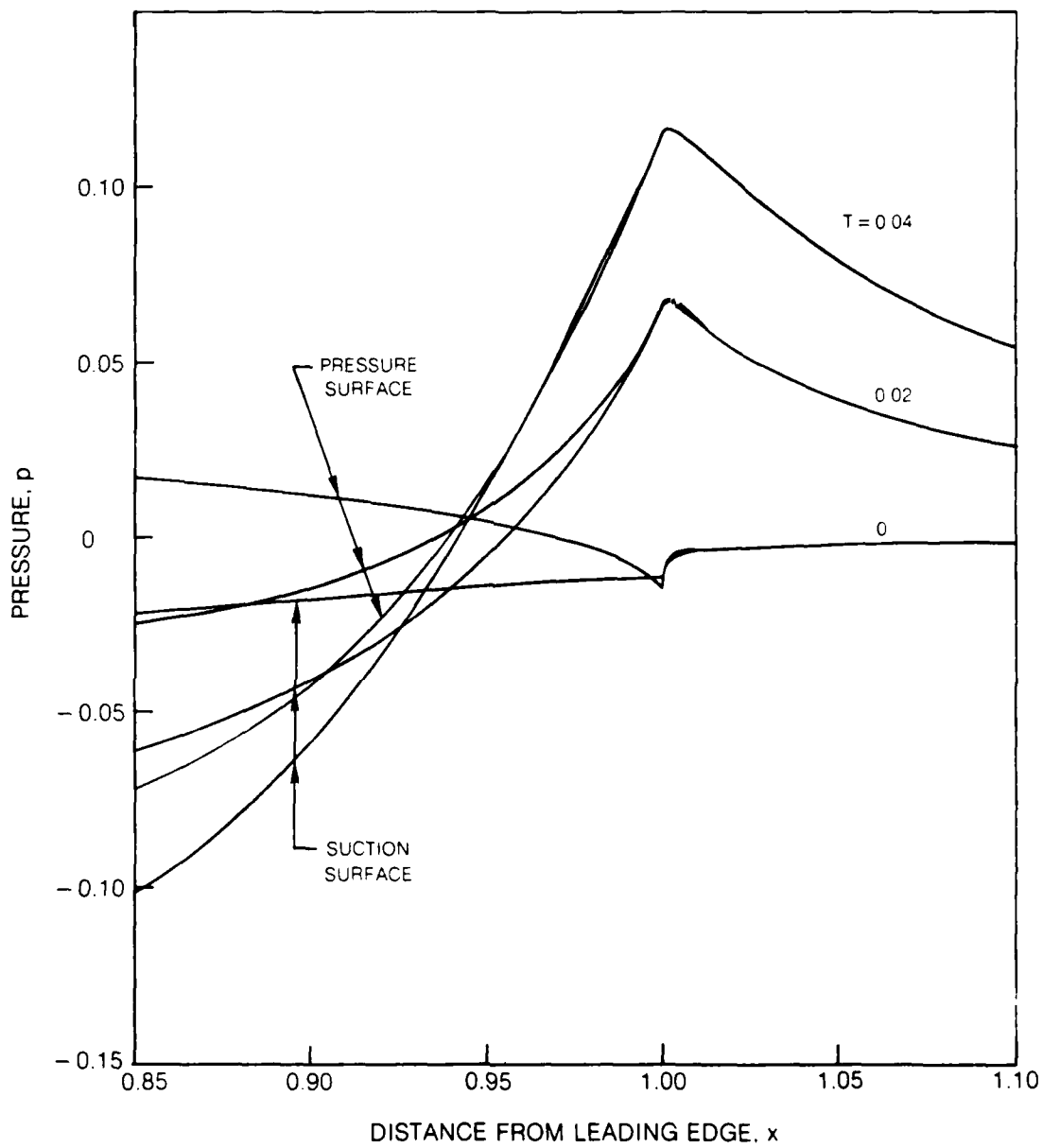


**Fig. 7 Asymmetric trailing-edge flow: effect of airfoil thickness;  $M_\infty = 0.7$ ,  $Re = 10^6$ ,  $\alpha = 0.05$ : c) Pressure distributions.**

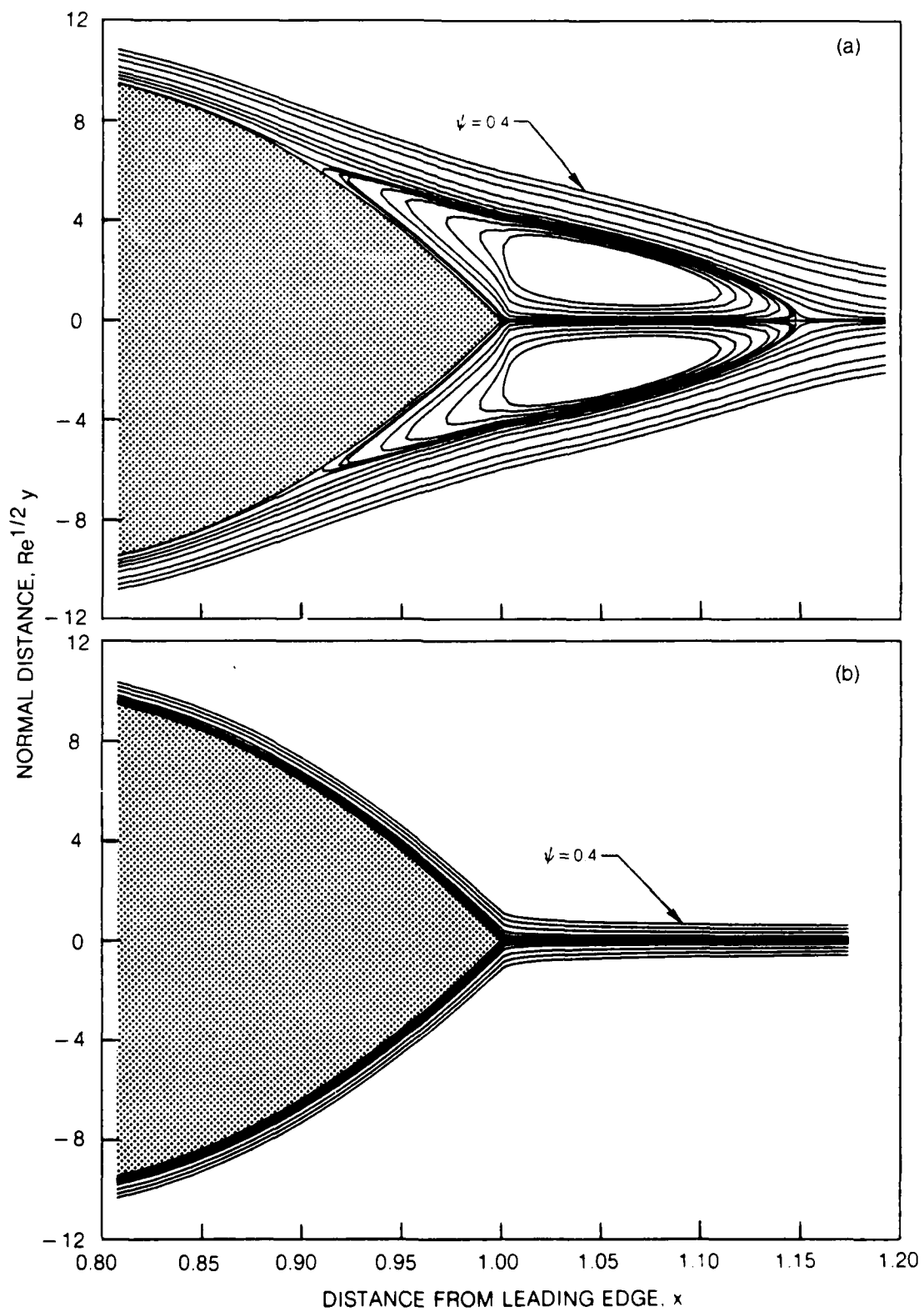


**Fig. 8 Effect of turbulence on trailing-edge streamline pattern for symmetric flow with  $M_\infty = 0.1$ ,  $Re = 10^6$ ,  $\alpha = 0$  and  $T = 0.02$ : (a) laminar flow (b) turbulent flow.**

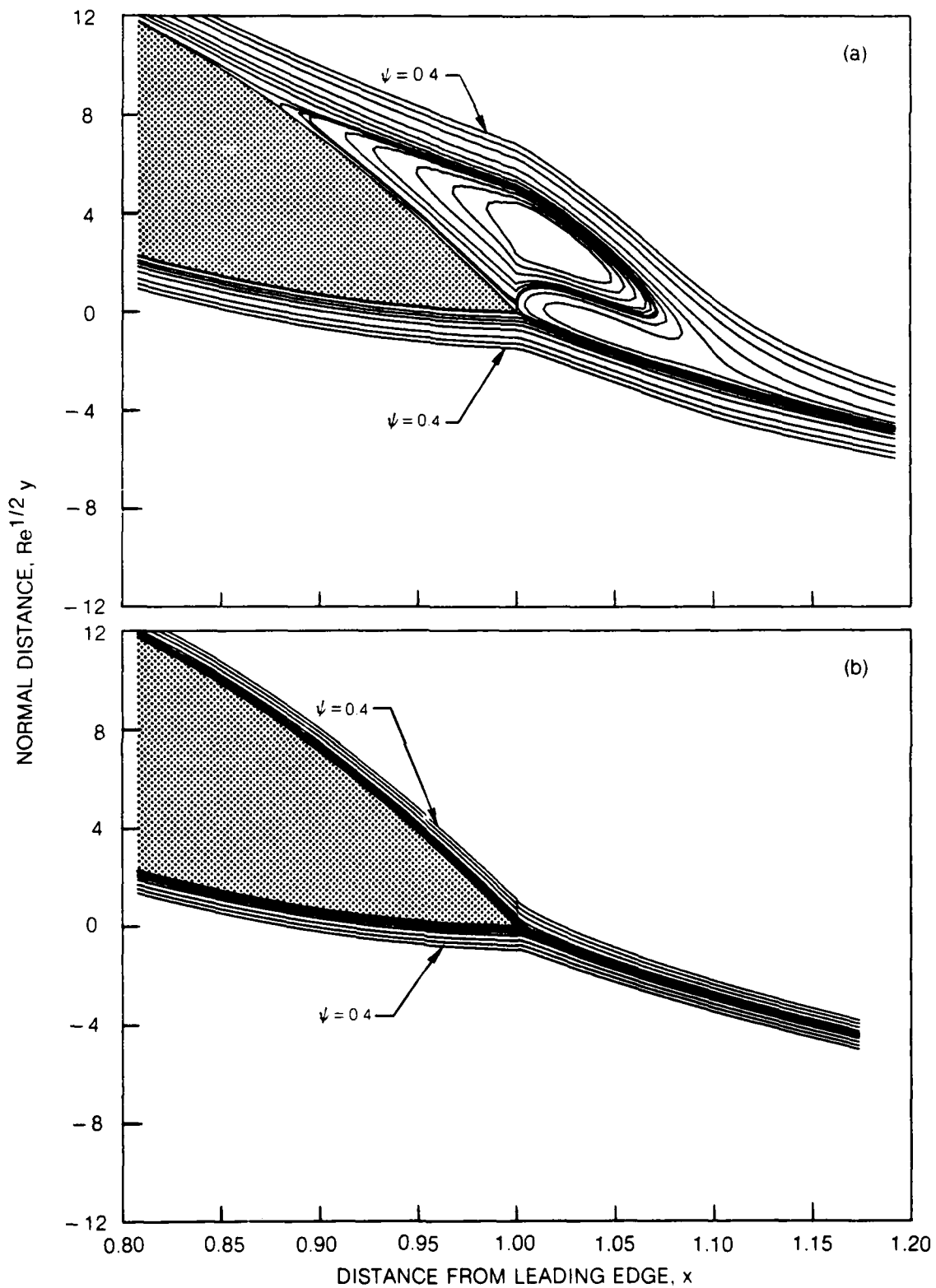


**Fig. 9** Effect of turbulence on trailing-edge streamline pattern for asymmetric flow with  $M_\infty = 0.1$ ,  $Re = 10^6$ ,  $\alpha = 0.07$  and  $T = 0.01$ : (a) laminar flow (b) turbulent flow.

DTIC

FILMED

4-86

END